# Characterization of nanometre-scale patterns on Cu(001) and Ag(001) by means of optical spectroscopy and high-resolution electron diffraction

Frank Everts

Samenstelling promotiecommissie:

| | |
|---|---|
| *Voorzitter:* | |
| prof. dr. G. van der Steenhoven | Universiteit Twente |
| *Promotor:* | |
| prof. dr. ir. B. Poelsema | Universiteit Twente |
| *Assistent-promotor:* | |
| dr. ir. H. Wormeester | Universiteit Twente |
| *Leden:* | |
| prof. dr. ir. H.J.W. Zandvliet | Universiteit Twente |
| prof. dr. ir. A.J. Huis in 't Veld | Universiteit Twente |
| prof. dr. J. Wollschläger | Universität Osnabrück |
| prof. dr. P. Zeppenfeld | Johannes Keppler University Linz |

This thesis is the result of work performed in the MESA+ Institute for Nanotechnology, Solid State Physics group, Faculty of Science and Technology at the University of Twente, The Netherlands.

This research was financially supported by NanoNed, a national nanotechnology program coordinated by the Dutch Ministry of Economic Affairs.
Nano Electronic Materials; Project TOE.7008

F. Everts
Characterization of nanometre-scale patterns on Cu(001) and Ag(001) by means of optical spectroscopy and high-resolution electron diffraction
ISBN: 978-90-365-3136-8

Published by the Solid State Physics Group, University of Twente
Printed by Printservice TU/e

Author email: f.everts@gmail.com

# CHARACTERIZATION OF NANOMETRE-SCALE PATTERNS ON CU(001) AND AG(001) BY MEANS OF OPTICAL SPECTROSCOPY AND HIGH-RESOLUTION ELECTRON DIFFRACTION

## Proefschrift

ter verkrijging van
de graad van doctor aan de Universiteit Twente,
op gezag van de rector magnificus,
prof. dr. H. Brinksma,
volgens besluit van het College voor Promoties
in het openbaar te verdedigen
op vrijdag 28 januari 2011 om 13.15 uur

door

Frank Everts
geboren op 30 december 1981
te Deventer

Dit proefschrift is goedgekeurd door de promotor:
prof. dr. ir. Bene Poelsema

en door de assistent-promotor:
dr. ir. Herbert Wormeester

# Contents

**1 Introduction 1**

1.1 Nanotechnology . . . . . 1
1.2 Pattern formation . . . . . 2
1.3 In-situ characterization . . . . . 4
1.4 Outline . . . . . 5

**2 Experimental 9**

2.1 UHV setup . . . . . 10
    2.1.1 Sample preparation . . . . . 11
    2.1.2 Ion gun . . . . . 12
    2.1.3 Deposition source . . . . . 12
2.2 SPA-LEED . . . . . 13
2.3 Reflectance Anisotropy Spectroscopy (RAS) . . . . . 17
    2.3.1 Setup . . . . . 17
    2.3.2 Surface strain . . . . . 20

**3 Large influence of the azimuth for near normal incidence ion impact on Cu(001) 23**

3.1 Introduction . . . . . 24
3.2 Experimental . . . . . 25
3.3 Angle of incidence and azimuthal dependence . . . . . 25
3.4 Summary . . . . . 30

**4 Optical anisotropy induced by ion bombardment of Ag(001) 33**
4.1 Introduction . . . 34
4.2 Experimental . . . 35
4.3 Results . . . 37
4.4 Quantitative analysis of the optical spectra . . . 42
4.5 Discussion . . . 44
4.6 Summary . . . 47

**5 Evolution of the anisotropy of ion induced nanopatterns on Ag(001) determined with Reflection Anisotropy Spectroscopy 49**
5.1 Introduction . . . 50
5.2 Experimental details . . . 51
5.3 Anisotropic optical response of nanostructured surfaces . . . 51
5.4 RAS Measurements . . . 53
5.5 LEED Measurements . . . 55
5.6 Determination of roughness evolution . . . 58
  5.6.1 Gaussian roughness distribution . . . 58
  5.6.2 Roughness evolution via EW model with Mullins diffusion . . . 61
5.7 Conclusion . . . 62

**6 Plasmon resonance shift during grazing incidence ion sputtering on Ag(001) 63**
6.1 Introduction . . . 64
6.2 Experimental results . . . 65
6.3 Optical characterisation of nanostructured surfaces . . . 65
6.4 Time evolution of the induced roughness . . . 70
6.5 Conclusion . . . 72

**7 Optical anisotropy induced by grazing incidence homoepitaxial growth on Ag(001) 73**
7.1 Grazing incidence deposition of Cu on Cu(001) . . . 74
7.2 Simulated optical response . . . 76
7.3 Measurements . . . 80
7.4 Conclusion . . . 82

**Summary 91**

**Samenvatting 95**

**List of publications** 98

**Dankwoord** 101

# Contents

# CHAPTER 1

# Introduction

## 1.1 Nanotechnology

Nanotechnology has become very important for our daily life, for instance through the major role of integrated circuits (IC's) in our society. These IC's contain literally millions of tiny structures and because of the need to make these chips smaller and faster, the size of these structures are in the order of a few nanometers nowadays. These IC's are typically made by optical lithography. For this technique every transistor, interconnection or any other structure, has to be designed carefully and reproduced very precisely. It is therefore a very time consuming and thus expensive technique. The current state of the art chips need this precision and are therefore bound to this lithography technique.

Nanometre size structures are also required to control surface cleaning, wettability and friction, as well as for optical coatings that enhance the efficiency of solar cells or for emitter arrays and pressure sensors. These applications require a much less well defined reproducibility of nanostructures. The self-organization of material on a surface can be used in such areas to create materials with new properties like superhydrophobicity, a combination of short range and long range periodicities [1], or light absorbers. Because of this wide range of applications and the low cost to cover large surface areas with a homogeneous pattern, it is a very interesting technique for industry. However, to be able to use this technique to its full potential, a fundamental understanding of the mechanisms behind this self organization is necessary.

A very promising tool for creation of homogeneous patterned surfaces is self organization by ion erosion or deposition. Regular and ordered arrays of nano size features can be prepared in this way, that exhibit special properties.

## 1.2 Pattern formation

Ripple formation by ion beam erosion was systematically studied for the first time by Navez et al. [2] in 1962. They noticed that even with a homogeneous beam, the removal of material from the surface is not homogeneous, but depends on the surface curvature. As a result, ripple patterns evolved on their glass substrates and depending on the polar angle of incidence, these ripples were oriented either perpendicular or parallel to the incoming ion beam. A large variety of different morphologies were observed in the earlier studies, including etch pits and pyramids [3]. Although there was a general understanding that this self-organization phenomenon was induced by the dependence of the sputter yield on the local topography, it took until the end of the eighties before a systematic theory was developed. The breakthrough in the understanding of ripple formation by ion erosion was by the continuum theory of Bradley and Harper (BH) [4]. This theory describes a balance between diffusion of species on a surface as described previously by Mullins [5] and sputtering of material in relation to the locally deposited power in the surface by an ion impact as developed by Sigmund. The BH-model explains many of the experimentally observed features such as the formation of ripples either perpendicular or parallel to the incoming ion beam, depending on the polar angle of incidence. The ripple wavelength depends exponentially on sample temperature and decreases for increasing ion energy. Although it is accurate for many experimental observations, it falls short in the cases where the crystallographic orientation also has an influence on ion erosion and diffusion. The BH-theory predicts an unlimited exponential increase in ripple amplitude, which is different from the observed saturation. It was clear that an extension of the BH-theory is necessary to describe specific cases.

Cuerno and Barabasi [6] added non-linear terms to the description, that depend on the penetration depth and angle of incidence. Their non-linear stochastic equation is from the class of anisotropic Kardar-Parisi-Zhang (KPZ) equations and describes the ripple formation on amorphous and semiconductor substrates quite well. Depending on the ion incidence angle, it predicts a ripple pattern oriented parallel to the plane of incidence for grazing incidence or perpendicular to the plane of incidence for sputtering close to the surface normal. For normal incidence sputtering there is no regular pattern predicted. Experiments show however, that for normal incidence ion bombardment on Cu(001) and Ag(001) regular square pit patterns [7,8], on Pt(111), Au(111) and Cu(111) regular hexagonal pit patterns [9–11] and on Ag(110) even ripple patterns evolve [12]. These patterns are resembling the underlying crystal, which is not incorporated in the model of Cuerno and Barabasi. These patterns were created on metal surfaces, that Rusponi et al [13] suggested to describe by adding anisotropic diffusion to the model. This results in an equation from the class of anisotropic Kuramoto-Sivashinsky (KS) equations. An important issue in these cases is the Ehrlich-Schwoebel (ES) barrier for interlayer mass transport. This barrier strongly influences the formation and shape of nanostructures.

The ripple formation on the various substrates seems to be the result of different underlying mechanisms, i.e. BH ripples and ES ripples. Although one mechanism is dominant for specific experimental conditions, it does not mean that the other mechanism is excluded. BH type ripples are observed on metal substrates and ripple patterns can be oriented according to the crystal structure on semiconductor substrates. Chan and Chason [14] created a phase diagram, describing the different regimes of patterned metal surfaces depending on the main experimental parameters of ion fluence and substrate temperature. Two main regimes are recognized, namely the erosive (BH) and the diffusive (ES) regimes. In the erosive regime the morphology is completely determined by the ion beam and diffusion plays a minor role. These morphologies typically occur at lower substrate temperatures. In the diffusive regime, the morphology is determined by the interplay between the erosion and the surface diffusion and thus the crystal structure.

To classify the evolution of ion induced nanostructures, mathematical tools from dynamic scaling theory are used. The surface evolution is characterized by the development of average distance between nanostructures $L$ and the surface roughness $\sigma^2$. In the initial non-stationary phase both the time evolution of these quantities are often observed to follow a power law, i.e. show dynamic scaling. The characteristic length increases with $L \sim t^n$ and the surface roughness increases with $\sigma \sim t^\beta$.

The value of these exponents is an indication of the type of morphology that evolves and can be derived from the equation describing the surface. For the KS equation the values are lower than for the KPZ equation [14]. Drotar et al. [15] determined values for exponents $\alpha$ and $\beta$ for statistically rough surfaces. One of the properties of the ion induced structures is periodicity $L$, which is a different property than the coherence length. Therefore exponent $n$ can not be compared with exponent $\alpha$. However, for the KS equation they found $\beta = 0.16 - 0.21$ and for the KPZ equation $\beta = 0.24$. Often different regimes with different exponents can be identified. Determination of the scaling exponents is only possible if enough data of the surface morphology is obtained as a function of time. Therefore a technique to determine the characteristic length scale $L$ and the surface roughness $\sigma$ is needed.

## 1.3 In-situ characterization

The determination of growth evolution via critical exponents is often done by repeating the experiment several times for different bombardment times. The morphological evolution is determined by characterizing the surface morphology ex-situ with a microscopic technique. The large drawback of this method is that it requires a multitude of measurements for the determination of just one parameter. Furthermore, the ex-situ morphology can differ from the morphology during ion erosion, which can lead to erroneous conclusions. An example of the latter was reported by Broekmann et al. [7]. A technique that allows to monitor the evolution of surface morphology during sputtering has therefore great advantages.

An obvious choice for in-situ characterization of surfaces is the use of photons, since they generally do not influence deposition or erosion experiments or are disturbed by the relative high pressure required for ion sputtering. A very powerful in-situ technique to obtain information about the (sub)surface morphology is grazing incidence X-ray diffraction. With X-ray diffraction the time evolution of orientation and periodicity of sputtered surfaces can be determined [16]. However, the geometry of the experimental setup is very restricted in x-ray experiments and the technique is restricted to a synchrotron facility. Therefore optical probes in the visible light are preferred.

Ion erosion can be used to create ripple patterns that have an obvious shape anisotropy compared to the smooth surface. This shape anisotropy results in a difference in optical reflection parallel or perpendicular to the ripples that can be sensitively registered with Reflectance Anisotropy Spectroscopy (RAS) [17]. The RAS technique was developed in the late eighties [18,19]. Since then it has been applied to many different areas in surface science. For example, Sun et al [20] showed that strain on a Cu(001) surface, induced by Co absorption, could be measured by RAS, or the determination of the growth mode of Ag on W(110) [21] or the deposition of (organic) molecules [22, 23].

To study the possibility of in-situ optical characterization of the ion erosion process, a Ag(001) substrate was chosen. The (001) orientation results in an isotropic start situation. This enables to attribute any observed optical anisotropy to the ion induced nanopattern. Patterning of a silver surface has the virtue of the observation of a surface plasmon whose resonance energy is a measure for the periodicity on the surface [24]. However, the analysis of optical spectra is not straightforward. In order to relate the optical spectra to the average morphological parameters, the Rayleigh Rice theory, a first order perturbation of the Maxwell theory is used.

Chan et al [25] already showed that the ripple amplitude and periodicity evolution can be monitored in-situ with a light scattering, a variation on the RAS instrument. The drawback is that this technique measures the scattered light coming of the sample, which is generally a small signal, compared to the strong signal of the reflected light that RAS measures. Using RAS as a morphological probe on cubic crystals also has the advantage that the signal is zero for a clean flat surface. Any measured signal can directly be contributed to the alteration of the surface.

## 1.4 Outline

The aim of this thesis is to obtain more information about the pattern formation by ion bombardment and homoepitaxy, by using an **in-situ** optical probe. Besides the elimination of the annealing effects, this also gives a better fundamental understanding of the processes that play a role in the pattern formation by self-organization. Besides the fundamental importance, this furthermore enables us to control the pattern formation process, which is a requirement for use of this technique in an industrial environment.

To exclude any outside influence all experiments were performed in ultra high vacuum. Chapter 2 describes the ultra high vacuum (UHV) setups that were used to obtain the experimental data in this thesis. It also explains how the high resolution Low Energy Electron Diffraction (HR-LEED) was used for facet determination and in the cleaning process, and how Reflectance Anisotropy Spectroscopy (RAS) was used as an optical probe, to obtain the in-situ optical information about the surface anisotropy.

Chapter 3 describes initial sputter experiments on the Cu(001) surface. The influence of the azimuthal orientation of the ion beam was investigated. A remarkable difference for bombardment along the $\langle 110 \rangle$ and the $\langle 100 \rangle$

was found. For sputtering along the ⟨100⟩ azimuth the fourfold symmetry is broken for a polar angle as small as 10°, whereas for sputtering along the ⟨110⟩ direction the fourfold symmetry is still intact for such small angles. For increasing polar angles, BH-behavior is observed for sputtering along ⟨100⟩, which is absent for sputtering along ⟨110⟩. These effects are attributed to the difference in penetration depth of the incoming ion for these azimuthal orientations.

Chapter 4 is the first chapter describing sputter experiments on the Ag(001) surface. It shows the results of the sputter experiment at an angle of incidence of the ion beam of 70°, resulting in semi-one dimensional features on the surface. For the analysis of the data, the Rayleigh Rice theory is introduced. Due to the one dimensional character of the ion induced features, the relation between optical spectra and surface morphology is possible via a one dimensional grating model. The periodicity of this grating shows a normal distribution. A fit to the spectra results in a description of the evolution of the amplitude and periodicity of the induced nanostructures. For both the critical exponent is determined.

By changing the position of the ion beam to a less grazing angle of incidence of 61.5°, a periodicity both in the plane of the incident ion beam as well as perpendicular to this can be observed. Chapter 5 shows how these more complex optical spectra can be described with the extended two dimensional Rayleigh-Rice approach. Even in this situation, a Gaussian distribution of the periodicity on the surface is the best way to describe the spectral density and enables the identification of two different periodicities in the two perpendicular directions on the surface. A fit to the recorded spectra allows to identify the evolution of the morphology.

The other limit is sputtering at a more grazing angle of incidence of the ion beam of 80°. The surface features become truly one dimensional, but more importantly, the periodicity drops typically below the 200 nm limit. A significant red shift is no longer detectable. The RRT model can be used, but it can simplified due to the limit of a large optical wavelength compared to the periodicity on the surface. This results in a model that shows that a discrimination between periodicity and roughness amplitude can no longer be made. The optical response is characterized by a skewed Lorentzian, whose amplitude and position change with sputter time. An analysis of these parameters as well as the width of the Lorentzian is made. Finally, chapter 7 shows an initial investigation of RAS for the study of grazing incidence growth. This growth mode has been the subject of intense studies in the solid state physics group. This has resulted in a series of simulations of the growth mode that shows highly anisotropic structures. These structures were confirmed experimentally. The potential of RAS to monitor this growth process in-situ, taking advantage of the grazing incidence induced anisotropy is investigated.

# CHAPTER 2

# Experimental

## 2.1 UHV setup

Two different ultra high vacuum (UHV) setups were used for the experiments described in this thesis. Setup “De Kater” was used for the experiments in chapters 3, 4, 5 and 6. The system has a base pressure below $10^{-10}$ mbar by a combination of a turbo pump and a liquid nitrogen cooled Ti sublimation pump. The schematic layout of this setup is shown in figure 2.1.

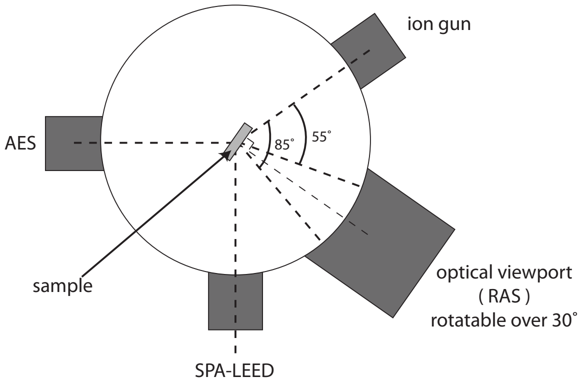

Figure 2.1: Schematic representation of the experimental setup ’de Kater’. The quadrupole (QP) is not shown on this diagram, but located at the upper level directly on the main chamber.

The following instruments are mounted on this system:

- **Spot Profile Analysis - Low Energy Electron Diffraction (SPA-LEED)** - high resolution LEED instrument manufactured by Omicron used for the investigation of facets on the surface after sample preparation.
- **Auger Electron Spectroscopy (AES)** - CMA analyser used for analysis of the surface composition (contamination), manufactured by Riber.
- **Ion gun** - sputter gun for cleaning and patterning purposes, manufactured by Leybold (type IQ12/63).
- **Reflectance Anisotropy Spectroscopy (RAS)** - home-built RAS setup to measure anisotropy in reflection. The optical access to the UHV is via a low stress quartz window.

- **Mass spectrometer** - for analysis of the rest gass composition in the main chamber, manufactured by Balzers (type QMG112).

The experiments in chapter 7 are performed on a newly built UHV system 'Eagle', also with a base pressure below $10^{-10}$ mbar. Again a combination of a turbopump and a liquid nitrogen cooled sublimation pump was used to achieve this pressure. The schematic layout of this system is shown in figure 2.2. The big advantage of this new setup is the fixed position of the optics and the moveable position of the deposition source. This results in an easier and more stable alignment and more flexibility. A different ion gun was used on this system for cleaning purposes and delivers a similar ion current gun as the ion gun on 'Kater'. SPA-LEED, AES (Varian 981-2601), mass spectrometer (SRS RGA200) and the home-built RAS setup are available on this system as well.

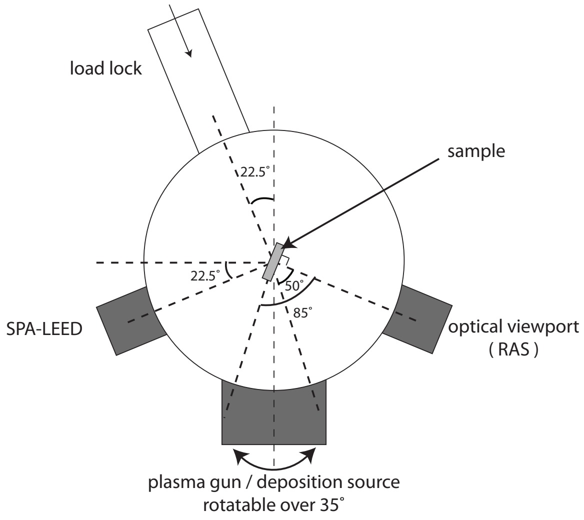

Figure 2.2: Schematic representation of the experimental setup 'Eagle'. Only the instruments on the lower sample position are shown. Instruments located in the top ring are: Auger Electron Spectroscopy (AES), quadrupole (QP), pressure gauge and an additional ion gun for cleaning purposes.

### 2.1.1 Sample preparation

Both the copper and silver samples were obtained from "Surface Preparation Laboratory" and the preparation before first use in the UHV systems is similar. The disc shaped samples with a diameter of 8mm were cut from a rod, in such a way that the sample surface is oriented along the (001) plane. The miss cut was below 1° and was achieved by mechanical etching and polishing steps. At this point, the substrates contain a too high level of contaminants, especially carbon and sulphur. To obtain a denuded contamination zone below the surface, the samples were annealed in a 1 atm H2 (5%)/Ar (95%) environment with a flow of 1 l/min for 48 hours. The copper sample was heated to 900K, while the silver sample was heated to a temperature of 800K. After this preparation, the samples were cleaned in the UHV system by sputter and anneal cycles. The sputtering is done with 800eV Argon ions at an polar angle of 45° for about an hour. The sample temperature is increased to 350K-450K during this bombardment for the silver and copper sample respectively. After the sputtering, the sample was annealed for at least 5 minutes to 800K-900K, to make sure all the implanted argon gas is released from the bulk. This cycle was repeated until no traces of contamination were detected anymore by AES, which means that the level of contamination is below 1%.

### 2.1.2 Ion gun

The output of the ion gun was calibrated by a so called Faraday cup. The collector plate in front of this Faraday cup is about 2.5 cm$^2$ and was used for rough alignment of the sample with respect to the ion gun. A hole in the middle of this front plate enabled exact ion current measurements at the back plate. The plates are located at the back side of the sample in the 'Kater', such that by rotating the manipulator by 180° it would result in an ion current measurement at the sample position. In the 'Eagle' the Faraday cup is located exactly 5 cm below the sample, facing the same direction as the sample surface. No bias voltages were used for measuring the ion flux, so the actual values measured are an upper limit, due to secondary electrons leaving the collector plate. Values were therefore mainly used for comparison and to estimate the order of magnitude of the ion gun output. All calibration measurements were done at normal incidence, unless otherwise stated.

### 2.1.3 Deposition source

A schematic diagram of the (silver) deposition source is shown in figure 2.3.

The thermal evaporation source consists of a small silver plate, mounted in a metal cylinder. Behind the plate a filament is positioned at a distance of a few mm. The filament can be elevated from ground by applying high

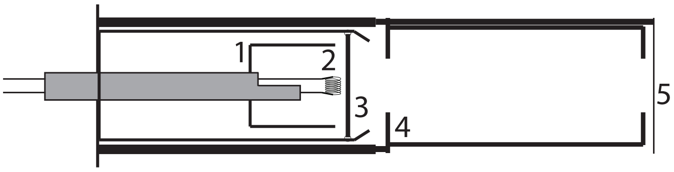

Figure 2.3: Schematic drawing of the deposition source: (1) Wehnelt cup (2) filament (3) sublimation disk (4) aperture (5) shutter

voltage, extracting more electrons and increase the heating capacity. To minimize deposition on other places than the sample surface, another metal cylinder is mounted on top of cylinder with the silver plate. This results in a smaller, less divergent beam. A shutter in front of this cylinder controls the exact deposition time. The metal block on which the cylinders are attached are water cooled, to prevent undesired heating of the environment, including cabling and connections. The source was kept at the operating temperature for at least 15 minutes before commencing the actual experiments, to ensure a constant deposition rate.

The calibration deposition rate of the source was done in a test system with a quartz crystal thickness monitor (Tectra MTM-10) was used. The distance source - quartz crystal was roughly half the distance source - sample and therefore the calibrated deposition rate was compensated with a factor 4. This calibration was done at normal incidence.

## 2.2 SPA-LEED

The spot profile analysis low energy electron diffraction (SPA-LEED) instrument was used for two purposes. After cleaning the sample, the domain size was checked by determining the width of the diffraction spots from the clean surface. By repeating the cleaning and anneal cycles, the domain size is increased until no decrease in spot size is observed anymore. Depending on the sample (Cu(001) or Ag(001)), the spots have a characteristic diameter on the freshly prepared surface. Figure 2.4 shows the typical LEED pattern of a clean Ag(001) surface and of a facetted surface. The FWHM of the $(0, 0)$ spot on the freshly prepared surface is approximately 0.3%.

The main purpose of the SPA-LEED instrument for the experiments in this thesis is obtaining information about the facets of the features on the surface. Note that these facets are not the thermodynamically facets the word is generally referring to. Throughout this thesis we use the word facet

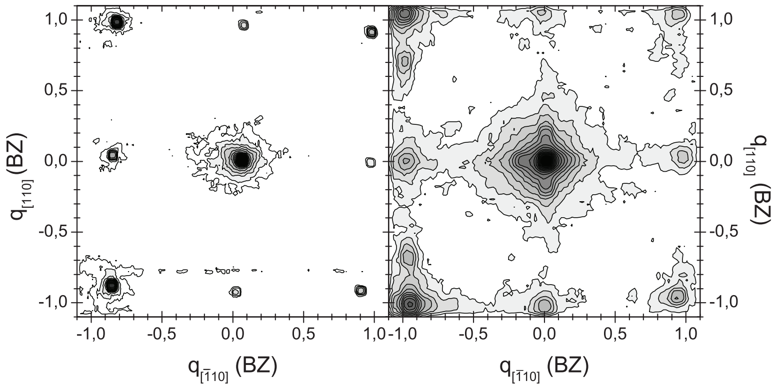

Figure 2.4: Typical LEED pattern of a freshly prepared Ag(001) sample and after a deposition experiment. Measurements are done with an electron energy of 220eV.

for very well defined facet like features. For a patterned surface, additional peaks appear near the $(0, 0)$ spot when measured close to the in phase condition. By analyzing the 2D scans of the diffraction pattern around the $(0, 0)$ spot as function of energy, not only the polar angle of the facet, but also the azimuthal orientation can be determined. Since in most experiments the structures were in the order of a few hundred nanometers, no peaks indicating the periodicity can be observed. A periodicity of 100 nm would give distance peaks at approximately 0.2% BZ, which is already below the diameter of the diffraction spots of the smooth surface and therefore not distinguishable. In figure 2.5 a series of 2D scans around the $(0, 0)$ spot is shown after patterning the Ag(001) surface by 80ML deposition of Ag with an angle of incidence of 80° and a sample temperature of 230K.

On the left-side of figure 2.6 all the facet peak positions of these 2D scans are plotted in one diagram. The in-plane movement of the facet peaks is a direct indication of the facet orientation on the surface. On the right side of figure 2.6, the in-plane distance to the $(0, 0)$ spot is plotted as function of perpendicular phase $S_{[001]}$ where $S_{[001]} = \frac{q_\perp \cdot d}{2\pi}$, $q_\perp$ is the perpendicular part of the change in wave vector of the electrons and $d$ is the interlayer distance of the sample surface. The slope is indicating the facet angle with respect to the surface. The specific facet orientations can be found by comparing the measured angle with the angles associated with the crystal geometry. Table 2.1 shows the angles with the surface plane for some low index facets.

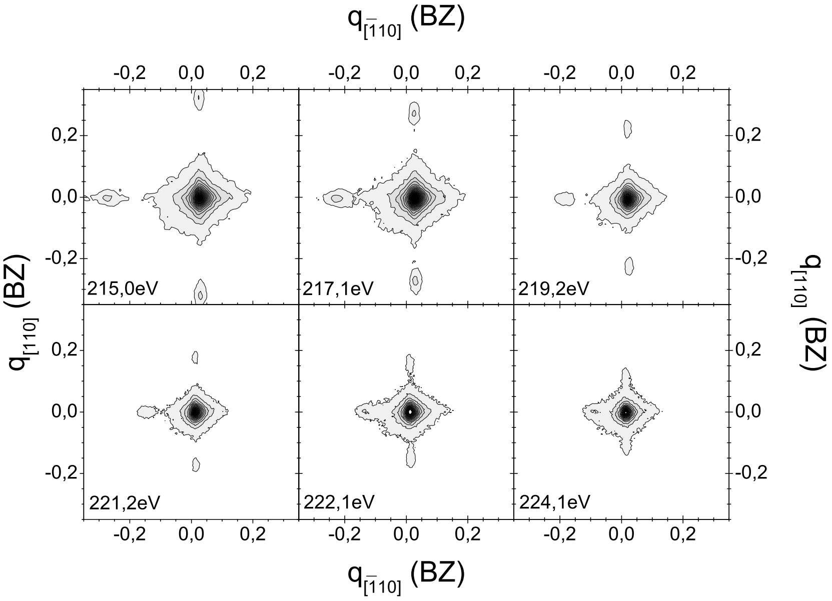

Figure 2.5: LEED 2D measurements on Ag(001) after 80ML deposition at 80° incidence and 230K, for different electron energies.

| facet | angle |
|---|---|
| (101) | 45.00° |
| (103) | 18.43° |
| (105) | 11.31° |
| (107) | 8.13° |

| facet | angle |
|---|---|
| (111) | 54.74° |
| (113) | 25.24° |
| (115) | 15.79° |
| (117) | 11.42° |

Table 2.1: The angle between the fcc(001) surface and some low index facets.

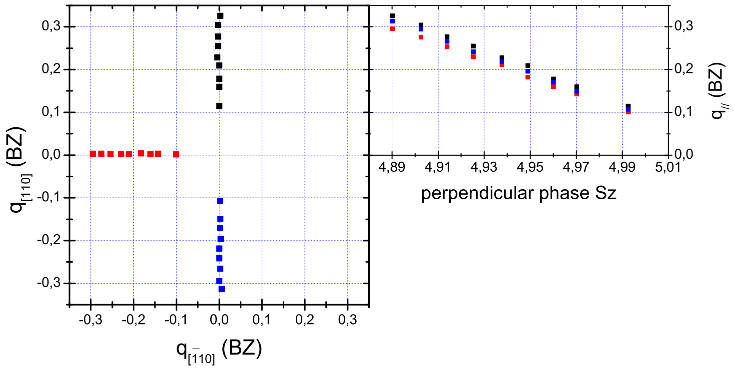

Figure 2.6: Facet peak positions in reciprocal space and distance to (0,0) peak as function of perpendicular phase $S_{[001]}$.

## 2.3 Reflectance Anisotropy Spectroscopy (RAS)

### 2.3.1 Setup

Reflectance Anisotropy Spectroscopy is used for the optical characterization of structured surfaces. For all experiments a homebuilt RAS setup of the Aspnes type [19] is used. This RAS setup could be mounted to any optical viewport, facing the sample surface at normal incidence. Measurements were always done at near normal incidence, of an incident angle $\leq 3°$.

In our RAS-setup, an xenon arc lamp (Osram) is used as an (unpolarized) light source. In this thesis all measurements are done on fcc(001) surfaces, with the incoming light polarized along the [100] direction by a polarizer (P1, Melles Griot Glan-Taylor 03 PTA 001), resulting in the reflectance difference between the $[1\overline{1}0]$ and the [110] directions (see fig 2.7). After reflection the light is modulated with a Photo-Elastic Modulator (Hinds PEM-90) at a frequency of 50KHz. Before detection a second polarizer (P2, same type as P1) along one of the probed direction is used, to get a normalized signal. The modulated signal is focussed on a fiber (Oceanoptics), which guides the signal to a photomultiplier (Denvers PR305). Before the photomultiplier, a monochromator (Oriel 7240) is selecting the wavelength (dispersion 6.4 nm/mm, 1200 l/mm). The signal from the photomultiplier is amplified with an IV-converter (Femto LCA-S). The sensitivity of the IV-converter is $-10MVA^{-1}$ and the bandwidth is 400kHz (well above the used modulation frequency of 50KHz). Before the signal is going to the lock-in amplifier (SRS830 LI or Anfatec ElockIn 204), the AC and DC parts of the signal are amplified separately (Hinds SCU-100). Finally, the AC part of the signal is analyzed with the lock in-amplifier, probing the first and second harmonic of the modulated signal. A computer is used to record the demodulated value from the lock in as well as the DC component.

The modulated signal coming into the lock in amplifier, is given by eq. 2.1 [19], where $\delta_1$, $\delta_2$ are the misalignment of the polarizers with respect to the PEM, $a_p$ the absorbance of the polarizers, $\Delta P$ the misalignment of the polarizer with respect to the direction on the sample exactly in between the two directions compared, and $\Delta C$ the misalignment of the PEM with respect to this same direction. By probing the first harmonic, the complex part of the reflectance difference can be probed and the second harmonic gives the real part of the reflectance difference. The measurements in this thesis are restricted to only the real part of the reflectance difference, since this contains most of the information and even a small residual strain in the viewport can influence the complex part of reflectance difference significantly

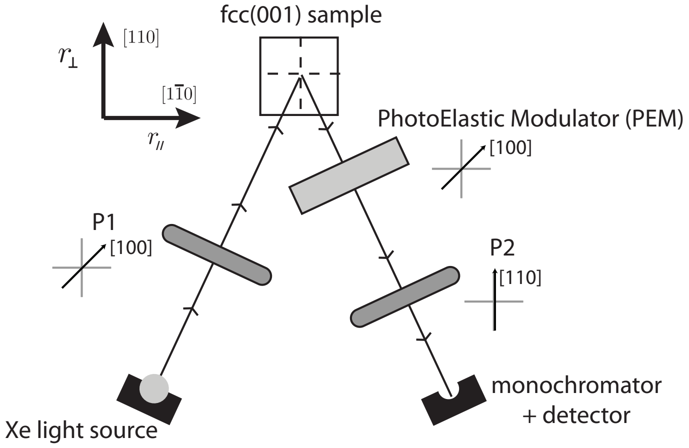

Figure 2.7: Schematic representation of the homebuilt RAS setup with orientatins of the optical components. Scans were performed with steps of $\Delta E = 0.02eV$. Light source is an unpolarized Xenon lamp with a spectral range of 1.8 - 5.5 eV. The modulating frequency of the PEM is $50kHz$.

[19, 26].

In general $\Delta C$ was minimized by aligning the [100] direction of the sample exactly along the optical axis of the PEM by looking at the LEED pattern. By rotating the first polarizer by hand, the value of $\Delta P$ was minimized. At the start of every experiment an isotropic Ag(001) surface was used. To compensate for residual chromatic abberations, a reference spectrum was measured, which was subtracted from all subsequent measurements. In this way, any signal coming from the misalignment of optical components is subtracted, since this signal due to misalignment can be considered linear over the whole optical range for small values.

$$\begin{aligned}\frac{V_{AC}}{V_{DC}} &= 2\cdot\left[\Im\left(\frac{\Delta r}{r}\right)+\delta_1\cos(2\theta_1)+\delta_2\cos(2\theta 2)-2a_p\right]\cdot J_1(\delta_c)\cdot\sin\omega t\\ &\quad +2\cdot\left[\Re\left(\frac{\Delta r}{r}\right)+2\Delta P+2\Delta C\right]\cdot J_2(\delta_c)\cdot\cos 2\omega t \qquad (2.1)\end{aligned}$$

The value of $\frac{\Delta r}{r}$ is obtained from the expression in eq. 2.2. The amplitude $V_{DC}$ and $V_{AC}$ have been corrected for their different amplification factors. The value of the two Bessel functions $J_2$ and $J_1$ are determined by the retardation of the PEM $\delta_{PEM}$, the wavelength of the PEM

$\lambda_{PEM}$ and the wavelength of the monochromator $\lambda_{light}$. By changing the PEM wavelength to the same value as the monochromator, the Bessel functions can be kept constant over the whole spectral range. By choosing $\delta_{PEM} = 0.383$, the value of $J_1$ will be zero. The whole expression reduces now to $(\Delta r/r) = (V_{AC}/V_{DC}) \cdot 1/(2 \cdot 0.432)$. The typical accuracy that can be achieved with our RAS setup is $2 \cdot 10^{-4}$ - $1 \cdot 10^{-3}$, depending on the UHV setup, the polarizers used and the photon energy.

$$\frac{\Delta r}{r} = \frac{(V_{AC}/V_{DC})}{2 \cdot J_2(\frac{2\pi\delta_{PEM} \cdot \lambda_{PEM}}{\lambda_{light}}) + (V_{AC}/V_{DC}) \cdot J_1(\frac{2\pi\delta_{PEM} \cdot \lambda_{PEM}}{\lambda_{light}})} \tag{2.2}$$

One of the main reasons for using RAS, is the ability to do in-situ measurements, in order to obtain more information about the dynamics during the nano-pattern creation. Since a photomultiplier is used in combination with a monochromator, the scanning time is depending on the optical range. Also the PEM has to be set for every specific wavelength, resulting in a lot of communication between the computer and PEM-controller, at the expense of (valuable) time. Therefore the measurements are a trade-off between sufficient optical range and the time resolution that can be achieved with this. The scanning speed can be greatly improved if the PEM is set at a constant specific wavelength and retardation for the whole scan. Only at the start of every scan communication with the PEM-controller is required. As already shown in equation 2.2, a fixed $\lambda_{PEM}$ implies a variable value for $J_1$ and $J_2$ as function of $\lambda_{light}$. This is corrected in the software by choosing appropriate values for $\delta_{PEM}$ and $\lambda_{PEM}$ (typically $\delta_{PEM} = 0.25$ and $\lambda_{PEM} = 476$ nm.

The error in the reflectance difference is depending strongly on both the strength of the lock-in signal and the DC voltage. The strength of the lock-in signal is mainly determined by the limitations of the optical components (mirrors and polarizers) and mechanical stability of the various parts. Since both the optical components and the mechanical stability are already optimized, further improvement of the sensitivity can be achieved by improving the DC signal. Instead of using a constant photomultiplier voltage $U_{PM}$, a PID-controller (Eurotherm 3216) was used to keep the DC voltage $U_{DC}$ constant. In figure 2.8a) the same measurement is shown in constant $U_{PM}$ mode (no adjustment) and constant $U_{DC}$ mode (adjusted $U_{PM}$). Figure 2.8b shows the photomultiplier voltage during the measurement of the last spectra. Despite the advantages of keeping $U_{DC}$ at a constant (high) level, there is not much of improvement in the noise level of the final RAS spectra.

However, an advantage of controlling the $U_{pm}$ during the experiment, is an extension of the optical range. The typical optical range that could be

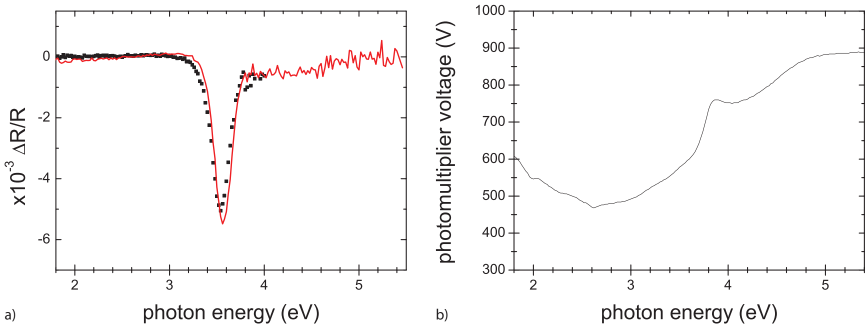

Figure 2.8: a). Comparison of a measurement without $U_{PM}$ adjustment (dots) and the extended spectrum with $U_{PM}$ adjustment, keeping the DC voltage at 0.5V (solid line). b) Photomultiplier voltage as function of photon energy.

measured by our RAS setup on the Ag(001) surface without any modification was 1.8 to 4.0eV. The lower limit is determined by the specifications of the photomultiplier, where the upper limit is due to the limited reflection of the silver surface. The reflection on the silver surface dramatically drops dramatically above 3.8 eV due to the interband transitions. By increasing the photomultiplier dynamically during measurements, this upper limit could be extended to about 5.5eV.

### 2.3.2 Surface strain

The extended optical range was used investigate the presence of anisotropic surface strain induced by the ion patterning of the sample surface. Sun et al [20] showed for copper that surface strain related oscillations, induced by oxygen adsorption, could be measured by RAS. Garfinkel et al [27] showed the strain induced change in reflectivity of silver by applying a small external force. They found that a strain of $e_{xx} = e_{yy} = 7 \times 10^{-5}$ results in a feature just below the edge for the intraband transitions at 3.84 eV, i.e. just above the position of the surface plasmon, a reflectivity change of $10^{-2}$ was recorded. Besides this enormous response, there are two other features as well, between 4 and 5eV, with a strength of $10^{-4}$.

The extended range of our RAS setup was used to check whether there is anisotropic surface strain, induced by grazing incidence sputtering. In figure 2.9 RAS spectra are shown for a ion bombarded silver surface after 7.5 hours of sputtering at a polar angle of 70° and a sample temperature of 370K. As expected the negative feature associated with the surface periodicity is coming below the surface plasmon energy. However, at photon energies above the surface plasmon energy, no strain related features could be observed. In none of our experiments any strain related features appeared, so in our sputter experiments the amount of strain is below the detection limit of our RAS setup. For small scale roughness, the relation between the reflectance difference and the change in dielectric function is given by eq. 2.3. Knowing that the the strain induced stress is related to the change in dielectric function by $\Delta\epsilon = We$ and from the work of Garfinkel it is known that for $e = 7 \cdot 10^{-5}$ a difference in reflection of $\Delta r/r = 10^{-2}$ is measured. This implies that the induced strain must lie below $e = 10^{-3}$ for a sensitivity of $10^{-4}$ with RAS.

$$\frac{\Delta r}{r} = \frac{-4\pi i d}{\lambda} \cdot \frac{\Delta\epsilon}{\epsilon_b - 1} \tag{2.3}$$

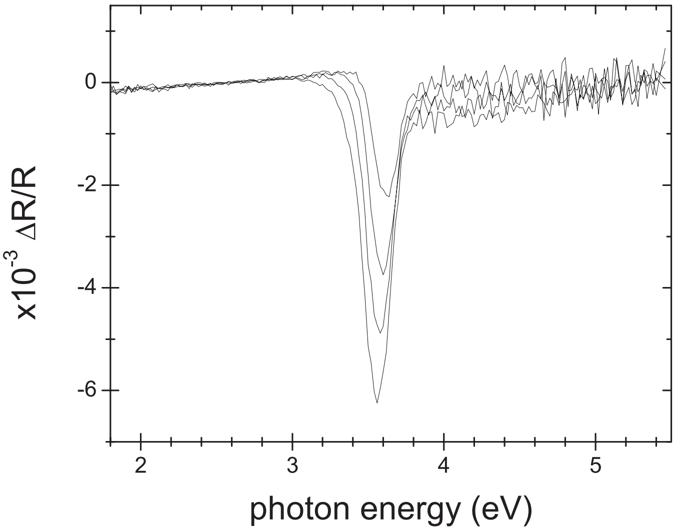

Figure 2.9: Extended RAS spectrum of an anisotropically patterned Ag(001) surface, showing no stress related features.

# CHAPTER 3

## Large influence of the azimuth for near normal incidence ion impact on Cu(001)

Ion bombardment induced surface structures on Cu(001) have been studied under conditions obeying the previously coined 'athermal Bradley-Harper (BH) region'. Off-normal ion impact along the $\langle 110\rangle$- and the $\langle 100\rangle$-azimuth at 200K gives rise to different high-resolution low energy electron diffraction patterns. Unanticipated and marked deviations from the inherent fourfold symmetry are obtained already at a polar angle of incidence as low as $10^\circ$. Experiments with 800eV $Ar^+$ ions (flux $6 \cdot 10^{12}$ ions $cm^{-2}$ $s^{-1}$, fluence $4.3 \cdot 10^{16}$ ions $cm^{-2}$) clearly show BH-behaviour for bombardment along [100] in contrast to bombardment along [110]. This observation is attributed to the higher probability for surface penetration of ions when incident along $\langle 100\rangle$. This remarkable finding is further corroborated by measurement at various energies between 0.2 and 2 keV along [100].

## 3.1 Introduction

Ion erosion has developed to a versatile technique for the preparation of nanostructures through self-organisation. A milestone in the development of this technique for nanopatterning was the theoretical description of the process by Bradley and Harper (BH) [4]. This approach predicts the formation of a ripple pattern as a result of an erosion instability. It explains that the ripple orientation is determined by the actual polar angle of incidence of the ions. For near normal incidence the ripples are oriented perpendicular to the plane of incidence of the ions, while at a certain critical angle a crossover towards a parallel orientation for more oblique ion incidence angle is observed [28]. A basic ingredient for this description involves isotropic diffusion of species on the surface. Patterns created on single crystalline metal surfaces provide insight in the influence of diffusion on the pattern formation. Experiments on Cu and Ag (110) surfaces explore the influence of a strong anisotropic diffusion on these surfaces [8, 13]. The patterns observed after normal incidence sputtering on Cu(001) were explained with the differences in the so-called Ehrlich-Schwoebel (ES) barrier for interlayer diffusion, which attenuates the mass transport over the ⟨110⟩- and ⟨100⟩-oriented step edges [7] differently. It was found that as a result of this difference the etched morphology shows kinetically stabilised {103}-facets at low substrate temperatures. In contrast, homoepitaxial growth leads to {113}-facets at similar temperatures [29]. As suggested previously [30], a strong post annealing effect of ion erosion induced structures on these (001) surfaces for temperatures above 250K was observed [7].

The BH instability leads to ripple patterns observed on very different surfaces [8, 31, 32]. However, for temperatures below 400K, a ripple pattern on both Cu and Ag(001) is only observed for grazing incidence sputtering [33–35]. As observed for normal incidence sputtering [7], the process leading to the etched structures is dominated by the ES barriers on these inherently isotropic surfaces. In their review, Chan and Chason [14] denoted this situation as the "ES instability" region. Ripple structures are also observed for higher ion fluxes and temperatures above 400K and this region was denoted as the "BH instability" region. Above 400K, the ES barrier associated with the ⟨110⟩ step edge (125meV, [36, 37]) no longer attenuates markedly the interlayer diffusion process. In the "BH instability" region also the characteristics of the BH instability, a change in ripple orientation with polar angle of incidence was observed for sputtering along the [100] azimuth. According to Chan and Chason, not only at high temperatures, but also at low temperatures the influence of the ES barrier can be suppressed. This results in enhanced interlayer mass transport at low temperature [38]. For the (001) surfaces of Cu and Ag, this leads to the proposition of a so-called ”athermal BH” region for temperatures below 200K [14]. In this temperature regime, diffusion is limited, but still active as observed from ripple formation at grazing incidence sputtering. The periodicity of the ripple pattern was shown to be linearly dependent on the ion energy. This dependence is the result of the short-lived thermal spike after ion impact [35]. This result showed that at low temperatures, the actual characteristics of the ion impact is much more pronounced in the observed pattern. In this paper we will show that a main characteristic of the BH instability, i.e. ripple rotation with polar angle of incidence is present in the ”athermal BH” region on the isotropic Cu(001) surface. Surprisingly however, this is only observed for ion impact in the {100}-plane, i.e. along the ⟨100⟩ azimuth and not for the ion impact in the {110}-plane (along the ⟨110⟩ azimuth). Since in both cases the major part of the ion energy is transferred to the crystal, this difference must be solely attributed to the difference in penetration depth of the ions along the {110}-plane and {100}-plane. Highly surprisingly, already at very small angles of incidence this difference is very pronounced.

## 3.2 Experimental

The experiments were performed in an ultra-high vacuum (UHV) chamber with a base pressure below $10^{-10}$ mbar. The Cu(001) crystal was cleaned with repeated sputter (Ar+, 800eV) anneal cycles [33]. The ion induced patterns were created by sputtering with argon ions along either the [110]- and [100]-azimuth at a temperature of 200K. After sputtering, the sample was rapidly cooled to below 130K to avoid as much as possible post annealing effects. High-resolution electron diffraction experiments were performed at this low temperature. For this purpose an Omicron Spot Profile Analysis Low Electron Energy Diffraction (SPA-LEED) system was used. Electron diffraction images were obtained for various electron energies to verify that features observed in the images were related to facets on the surface and to extract the actual facet orientation.

## 3.3 Angle of incidence and azimuthal dependence

Figure 3.1 shows electron diffraction images obtained for sputtering along both the [110] or [100] azimuth for various polar angles of incidence $\theta$. All images were recorded after 2 hrs. sputtering with 800eV Ar ions on the

Cu(001) surface held at a temperature of 200K. At normal incidence, an ion current of $1\mu A$ cm$^{-2}$ is measured. The images for various angles of incidence obtained after sputtering along the [110] azimuth are very similar to previously reported results [34]. The patterns around normal incidence show a strictly fourfold symmetric pattern with diffraction features along the [100] azimuth. These features represent the (103)-facets associated with inverse pyramid structures created on this surface. Measurements show that the position of these features in reciprocal space varies with the electron energy [7]. For all images in this chapter, an electron energy of 275eV was used (perpendicular phase $S_Z = 4.91$).

Sputtering along the [100] azimuth results in very different electron diffraction images. Already a polar angle of incidence of $\theta = 10°$ is sufficient to break the fourfold symmetry completely. This is in marked contrast with the result along the [110] azimuth. It is also remarkable that a small change in angle of incidence already results in such large differences. The two strong features in the azimuth direction of the sputter beam ( [100] ) indicate the formation of two well defined (103)-facets. For $\theta = 10°$ only weak facet spots are observed in the direction perpendicular to the ion beam ( [010] ). A slight increase of the incidence angle to $\theta = 20°$ virtually removes the intensity of these faint features. Only the two strong facet features in the direction parallel to the ion beam (see arrows) are observed. This indicates that a ripple like structure perpendicular to the plane of the incident ion beam is created. The similar intensity of the two facet features changes around an incidence angle of $\theta = 40°$, while for $\theta = 60°$ a transition stage is observed. For $\theta = 70°$ an electron image representative for a ripple structure parallel to the plane of the incident ion beam is observed. This change in ripple orientation with polar incidence angle for ion sputtering along the [100] azimuth is consistent with the main prediction of the BH theory, indicating a critical angle for orientation of around 60°. Ion bombardment along ⟨110⟩ leads to drastically different results. Only at grazing incidence ($\theta > 70°$) ripples oriented parallel to ⟨110⟩ are formed. At smaller polar angles no ripple formation is detected and thus no evidence for BH-behaviour is present in the [110] data. Summarizing, an "athermal BH" region in the sputter phase diagram for sputtering along the ⟨100⟩ azimuth is found.

To elucidate further the difference between sputtering along the two azimuth directions, the influence of the ion energy on the pattern formation for sputtering along the [100] azimuth was investigated. Figure 3.2a) shows the SPA-LEED measurements after sputtering at $\theta = 20°$ with an ion energy of 200eV and 800eV. For $\theta = 20°$ faint side peaks of the broken fourfold symmetry are visible, which makes it easier to identify the influence of the

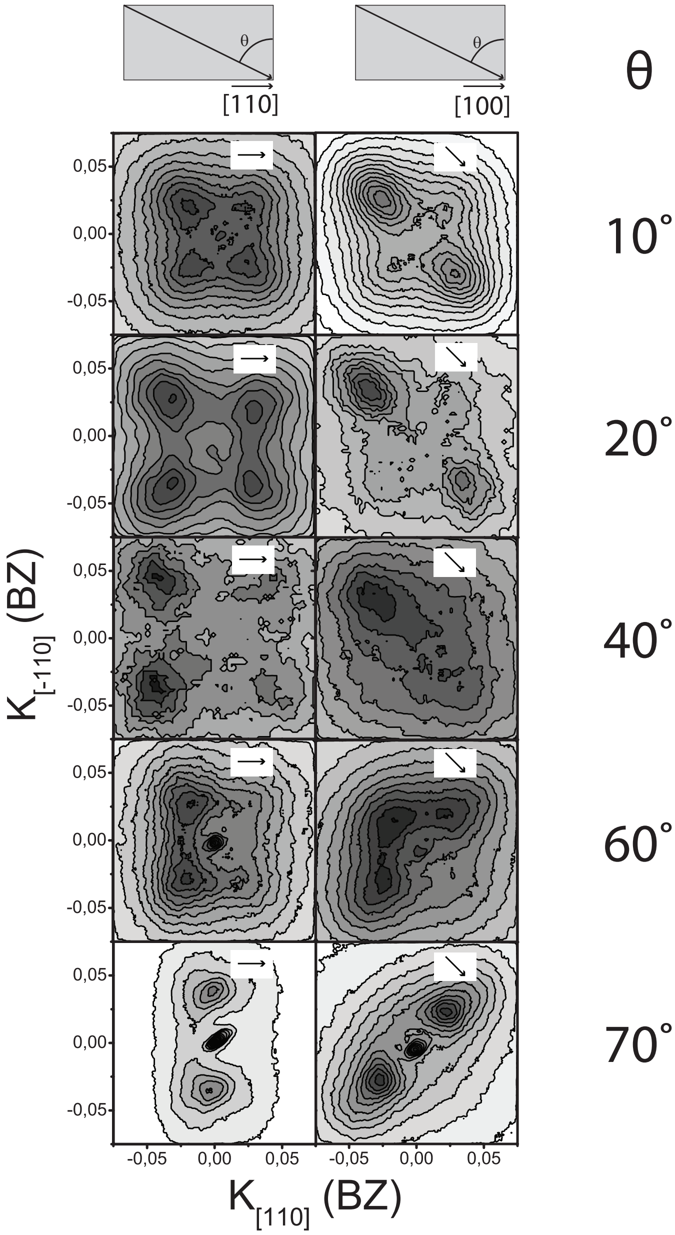

Figure 3.1: HR-LEED measurements (contour plots of the intensity; arbitrary grey scales) at an electron energy of 275 eV after 2hrs of sputtering at 200K as a function of the polar angle of incidence from $\theta = 10°$ to $70°$. Shown are results for bombardment along the [110] (left) and [100] (right) directions of the Cu(001) surface. The ion energy was 800eV and the ion current was $1\mu A$ cm $^{-2}$, measured at normal incidence. The arrows indicate the azimuth direction of incidence.

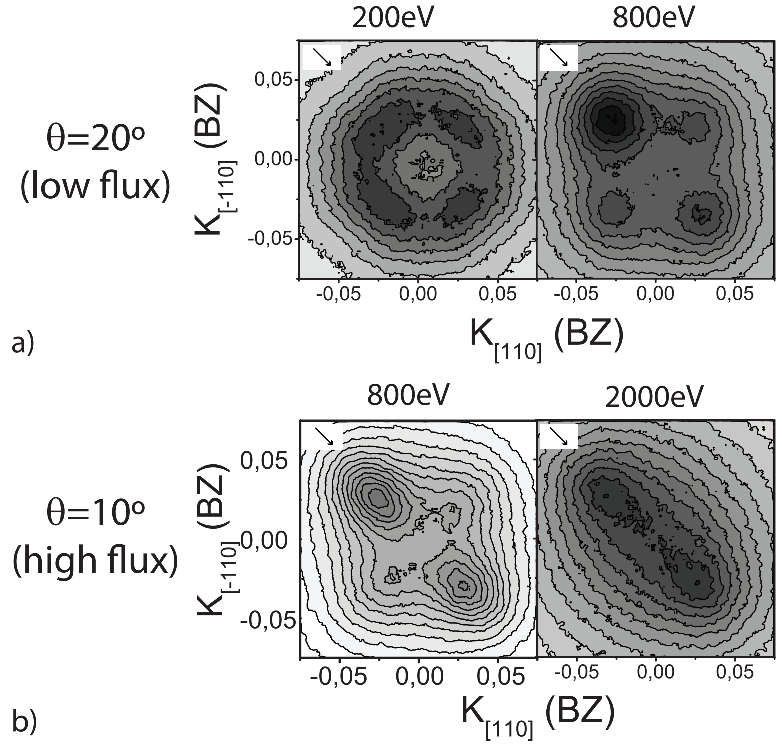

Figure 3.2: HR-LEED measurements at an electron energy of 275 eV after Ar ion bombardment at a temperature of 200K along the [100] azimuth. a) Sputtering at $\theta = 20^\circ$ for 22 hrs with with a flux of $0.55 \times 10^{12}$ ions cm$^{-2}$ s$^{-1}$. The ion energies are 200eV and 800eV respectively. b) Sputtering with $\theta = 10^\circ$ for 2 hrs with a flux of $6 \times 10^{12}$ ions cm$^{-2}$ s$^{-1}$. The energies are 800eV and 2keV respectively.

decrease in ion energy. The much lower flux of the ion gun at 200 eV ($0.55 \times 10^{12}$ ions cm$^{-2}$ s$^{-1}$), was compensated by sputtering for 22 hrs., leading to the same fluence as for the data displayed in fig. 3.1. These low ion flux results illustrate that the ion energy indeed strongly influences the symmetry of the observed diffraction pattern. The result obtained with 800 eV ions also shows pronounced features in the [100] direction. In contrast to the higher flux situation at this polar angle of incidence (see fig. 3.1) weaker features in the direction perpendicular to the plane of the incident ion beam i.e. along $[1\bar{1}0]$ can be distinguished. This shows resemblance to the observation for $\theta = 10^\circ$ in fig. 3.2b. The sputtering at 200 eV results in a very different pattern, showing a fourfold symmetry akin to those obtained for sputtering at normal incidence or at near normal incidence along the

[110] azimuth. The facet features are less pronounced and actually instead of 4 facet peaks 8 features may be discerned. The latter is probably the result of the smaller interlayer mass transport experienced for the extended sputter time. In this situation a tendency to strive for the more energetically favourable ⟨110⟩ step edges is expected [7] and a mixed situation results. The presence of the fourfold symmetry after sputtering with 200 eV energy ions shows that the details of the ion impact, in particular the ion energy, determine the pattern formation in the "athermal BH" region.

Figure 3.2b) shows the diffraction images for sputtering at $\theta = 10°$ along the [100] azimuth with ion energies of 800eV and 2keV. Again, the faint side peaks of the broken fourfold symmetry are visible, which makes it easier to identify the influence of the increase in ion energy. The diffraction image after sputtering at 800 eV shows both prominent facet features along [100] and very weak features along [010]. An increase of the ion energy to 2 keV results in a total vanishing of the weak features, leading to an even more anisotropic morphology.

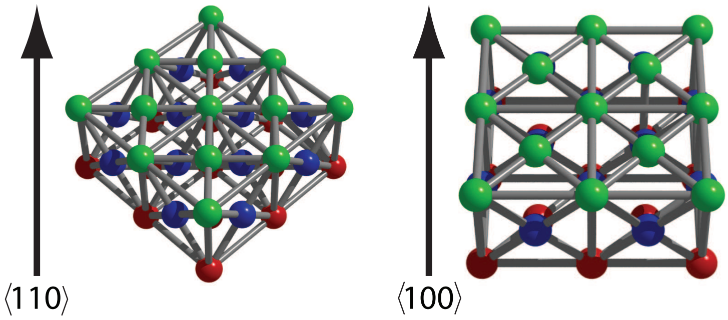

Figure 3.3: Crystallographic orientations of the fcc(001) crystal at a viewing angle of 20°. The first three layers are indicated with green, blue and red (see text).

The results shown in Figs. 3.1 and 3.2 illustrate that the details of ion impact itself play a crucial role as evidenced by the different degree of anisotropy in the diffraction patterns. The angle of incidence (both polar and azimuth) as well as the ion energy, and thus the penetration depth of the ion into the crystal, determine the details of this ion impact. The differences observed in the data in fig. 3.1 obtained after sputtering with the same ion energy of 800 eV and the same polar angle of incidence show that the azimuth angle has a profound influence, related to sputtering along the $\langle 110 \rangle$ and $\langle 100 \rangle$ azimuth.

There is a huge difference in sputter efficiency for (near) normal incidence sputtering along the two azimuthal directions. This is directly related to the penetration of the ions in the crystal and thus the possibility to reach deeper layers. Channeling is the easiest way to achieve this. At near normal incidence, there is channeling possible for both azimuthal directions. Obviously, along the $\langle 110 \rangle$ azimuthal direction planar channeling is possible in the $\{110\}$ plane and along the $\langle 100 \rangle$ azimuthal direction planar channeling is possible in the $\{100\}$ plane. Although at first sight these planar channels look equivalent, this is not the case. Since the distance between atoms along the $\langle 110 \rangle$ azimuth is smaller ($1.28\mathring{A}$) than along the $\langle 100 \rangle$ direction ($1.81\mathring{A}$), the distance between the $\{110\}$ planes is also smaller than the distance between the $\{100\}$ planes. Therefore, planar channeling close to normal incidence will be much easier along the $\langle 100 \rangle$ direction, which enhances the sputter efficiency dramatically.

Not only at near normal incidence, but also for increasing polar angle channeling can occur. For sputtering along the $\langle 110 \rangle$ azimuth there is a $\{111\}$ planar channel at an angle of 35.3° accessed. With the interlayer distance of $2.55\mathring{A}$ the probability for penetrating more deeply into the crystal becomes relatively high. For sputtering along the $\langle 100 \rangle$ azimuth, at an angle of 45° with the surface normal, there is an axial channel along the $\langle 101 \rangle$ direction. In both cases this is the polar angle were a transition in diffraction pattern was observed.

## 3.4 Summary

Surprisingly, the azimuthal orientation was found to play already a prominent role on the etch pattern formation for near normal incident ion bombardment on Cu(001) with 800 eV $Ar^+$ ions. A profound difference in the symmetry of the electron diffraction pattern is observed for a polar angle of incidence of only 10° between sputtering along the [110] and the [100] azimuth. In contrast, bombardment along the [110] azimuth shows a gradual transition from the fourfold symmetric diffraction pattern as observed for normal incidence sputtering to a twofold symmetric diffraction pattern observed for oblique incident sputtering. Bombardment along the [100] azimuth shows already for near normal incidence a twofold symmetry pattern. The orientation of the ripples associated with this pattern rotates from perpendicular to the ion beam to parallel to the ion beam with increasing ion incidence angle. This behaviour is expected within the Bradley-Harper description of ion beam induced roughening. The remarkable difference in behaviour for sputtering along the $\langle 110 \rangle$ and $\langle 100 \rangle$ azimuth is solely caused by a difference in penetration depth of the incoming ion, due to the screening by atoms in the outermost layer. Experiments with different ion energies verify the pronounced influence of the penetration depth on the development of the surface morphology.

# CHAPTER 4

# Optical anisotropy induced by ion bombardment of Ag(001)

Grazing incidence ion bombardment results in the formation of nanoripples that induce an anisotropic optical reflection The evolution of the reflectance anisotropy has been monitored in-situ with reflectance anisotropy spectroscopy. The Rayleigh-Rice theory (RRT) has been used to analyze the optical spectra quantitatively and provides the evolution of the average ripple period and root mean squared surface roughness. After an incipient phase, both the increase of the periodicity and the roughness vary roughly with the square root of the sputter time. Additional high-resolution low-energy electron diffraction (HR-LEED) measurements have been performed to characterize details of the average structure created by ion bombardment.

## 4.1 Introduction

In the last decade, ion beam erosion has emerged as a versatile technique for the creation of nano-patterns [7, 8, 14, 35, 39, 40]. This technique has great potential, since it enables a fast and easy way to create large homogeneous areas with highly ordered features. Most common is the formation of a pattern with a height modulation in one direction, a nanoripple pattern. After a sufficient ion fluence during off-normal ion bombardment, a stationary situation results, characterized by the periodicity of the nanoripples. The latter is determined by the combination of the diffusive properties of species on the surface, the polar angle of incidence and the incident ion flux, mass and energy [4, 6]. This periodicity in the stationary situation has been observed on many surfaces, among them the crystalline Cu(001) surface [25, 35]. This evolution has been compared to the aeolus evolution of sand dunes by Aste and Valbusa [41]. They explained the evolution of the ripple structure with the variation in erosion amplitude of various wavelengths present on the surface that are triggered by random fluctuations. However, the evolution of the periodicity and surface roughness before the stationary situation is achieved has only been the subject of a limited number of experimental studies [13, 42–44]. In-situ experimental investigations of the ripple evolution are hampered by the ion beam used in the erosion process. It requires a gas pressures and geometries that are not compatible with many microscopy and diffraction techniques. In this article we will show that optical metrology provides an excellent method for in-situ characterisation of the average ripple period, the surface roughness and their evolution under these circumstances.

Optical characterization of ripple formation on the Cu(001) surface by ion beam erosion was already performed by Chan et al. [25]. With Light Scattering Spectroscopy (LiSSp) they were able to characterize the periodicity of ripples with an average periodicity between 300 and 2000 nm. However, the LiSSp method detects light scattered at angles different from the specular beam. This implies that at least two viewports are required and their orientation limits the periodicities that can be measured. Furthermore, it relies on the detection of a weak signal while it is also not sensitive to roughness below the diffraction limit. Reflective anisotropy spectroscopy (RAS) is a technique that can overcome these restrictions. It has been introduced by Aspnes et al. [18, 19] to study the above-band gap anisotropy of cubic semiconductors and has matured in a versatile technique for the analysis of optical anisotropy at a surface by reflection of a light beam at normal incidence [17]. The ripple pattern induced by ion bombardment induces a difference in reflection for light polarized parallel and perpendicular to the ripple pattern. Effective medium theories that describe the dielectric function of a layer as a result of a heterogeneity on a length scale below the diffraction limit often take the specific geometry in to account [45]. The 1D ripple pattern can be viewed as a lamellar structure. A difference in effective dielectric function parallel and perpendicular to the lamella was already derived by Wien. This implies that RAS is sensitive to anisotropic structures with a periodicity below the diffraction limit. This technique has already been employed by Martin et al. [46] to study ion erosion. They limited their study to the effects of ion bombardment on the optical and electronic properties of the intrinsically anisotropic Cu(110).

In this work, we present a study of the ripple formation through ion bombardment on the intrinsically *isotropic* Ag(001) surface. The ripple formation on the Ag(001) surface has been studied for two reasons. Firstly, the surface shows no anisotropy before ion sputtering. Any observed anisotropy is therefore directly related to the ion bombardment. With an appropriate analysis, the observed anisotropy can thus be related quantitatively to the average ripple periodicity and rms roughness upon ion erosion. The second reason for using this surface is the presence of strong plasmonic effects. The strong coupling between the wavelength of the incident light and the periodic length scale of features on the surface induces an absorption at a photon energy that is very characteristic for the specific ripple period. Therefore, for features of even a few monolayers deep, the optical anisotropy is already significant. This enables the in-situ monitoring of the pattern formation directly from the start and makes RAS a sensitive tool for the analysis of surface morphology. The ripple formation has been studied at a polar angle of incidence of the ion beam of 70° and 80°. Additional electron diffraction experiments reveal that at a polar angle of 70° the etch structures still show persistent 2D character [42], although the optical measurements are sensitive for the ripple periodicity only and not for the ripple length for the range of temperatures studied. At 80° a 1D ripple pattern is observed with both optical and electron diffraction methods.

## 4.2 Experimental

The experiments were performed in an ultra-high vacuum (UHV) chamber with a base pressure below $10^{-10}$ mbar. The cleaning procedure of the Ag(001) crystal consisted of 45 minutes of sputtering under an angle of 45° along the crystallographic $[\bar{1}10]$ direction and subsequent annealing at 700K for 30 minutes. The cleanliness of the surface was monitored by Auger spectroscopy until no traces of surface contamination could be found, which ensures a contamination level below about one atomic percent. The system was further equipped with an Omicron Spot Profile Analysis Low Electron Energy Diffraction (SPA-LEED) system. At in-phase conditions, the Bragg-peak had a width of about 0.4% Brillouin zone (BZ), indicating an average terrace width of about 100 nm, without any preferential direction for a freshly prepared sample. This instrument was also used to characterize the structures after ion bombardment.

A homebuilt RAS setup (Fig. 4.1) was used in our experiments very similar to the one described by Aspnes et al [19]. A Xe light source was used to create a near parallel light beam. This beam was linearly polarized along the crystallographic [010] direction of the substrate before entering the UHV chamber through a strain free quartz window. The beam was reflected by the substrate at a near normal angle and passed through the same UHV window. The specular reflected beam passed through a photo elastic modulator (type Hinds PEM-90) also oriented in the [010] with respect to the substrate. With this setup the change in polarization by the surface can be probed. Both the intensity of the first and second harmonic of the modulated signal with respect to the DC intensity are measured with a lock-in technique. This provides both the imaginary and the real part of the reflectance difference, which is defined as:

$$\frac{\Delta r}{r} = 2\left(\frac{r_{[110]} - r_{[\bar{1}10]}}{r_{[110]} + r_{[\bar{1}10]}}\right) \tag{4.1}$$

with $r_{[110]}$ and $r_{[\bar{1}10]}$ the reflectivity of the Ag(001) surface along the [110] and [$\bar{1}$10] azimuth, respectively. The precision achieved in using this setup amounts to $\Delta r/r = 5\times10^{-5}$, while a spectral range of 226nm - 830nm (1.5eV - 5.5eV) is accessible. A measurement of this complete spectral range takes approximately 18 minutes.

Grazing incidence ion bombardment along the [$\bar{1}$10] crystallographic direction has been performed with a polar angle of incidence of $\theta_i = 70°$ and 80° with the surface normal. The energy of the $Ar^+$ ions is 2 keV and a flux of $5\mu A$ cm $^{-2}$ s$^{-1}$ ($3\times10^{13}$ ions cm$^{-2}$ s$^{-1}$ ) has been used. This flux is equivalent to an impingement rate of 1.5 MLE/min. One Monolayer Equivalent (MLE) is defined as the ion dose required to have a surface atom hit by one incident ion on average. The sputter time in all experiments is 18 hours, resulting in a fluence of $2\times10^{18}$ ions cm$^{-2}$. During the ion bombardment, a RAS spectrum is taken every 20 minutes. The sample temperature is kept constant with an accuracy of ±2K in the range of 300K - 450K. Directly after switching off the ion beam, the sample is cooled to below 130K to ”freeze in” the obtained ripple-pattern. High-resolution electron diffraction experiments have been performed at this temperature, to obtain additional information about the shape of the created surface features, including their facets.

Before ion bombardment, a RAS spectrum is taken of the optically isotropic clean Ag(001) surface. Weak deviations from zero anisotropy are attributed to systematic errors and used to correct the measurements. By rotating the clean sample by 90°, the sign and strength of the optical anisotropy was very similar, which confirms that this signal can indeed be attributed to systematic errors of the set-up.

## 4.3 Results

The evolution of the RAS spectra during ion bombardment is shown in figs. 4.2a to 4.2d for different sample temperatures for a polar angle of incidence of 70°. The interval between successive spectra is 1 hour. The ion bombardment results in a plasmonic feature with a strength increasing with sputter time. For temperatures up to 320K, the energy position of this plasmonic feature is similar to the surface plasmon energy of Ag, which is about 3.70eV and only slightly temperature dependent [47]. The increase in signal strength is a result of a significant roughening of the surface while the fixed position indicates that the periodicity of this roughness is below 200nm. For higher temperatures, a different behavior is observed. The increasing signal strength is accompanied by a redshift of the plasmon energy peak and also peak broadening is visible. The redshift indicates an increase in

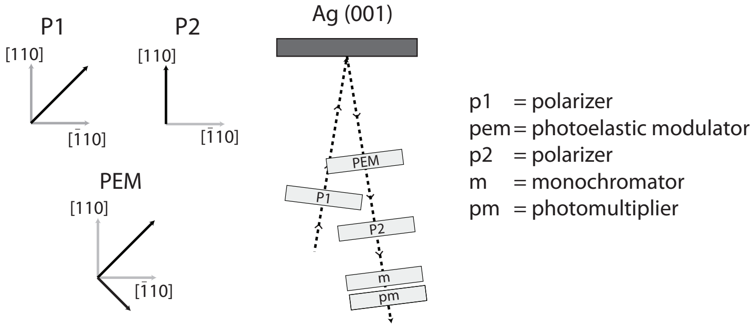

Figure 4.1: Schematical overview RAS setup.

the average distance between ripples. As expected, the ripple periodicity increases during the sputtering. With increasing sample temperature, the lateral dimensions also increase and thus this shift becomes increasingly more distinct. The peak broadening indicates a widening lateral periodicity distribution on the surface. At the low and high energy ends of the spectra, the noise level increases due to a decrease of the reflected intensity.

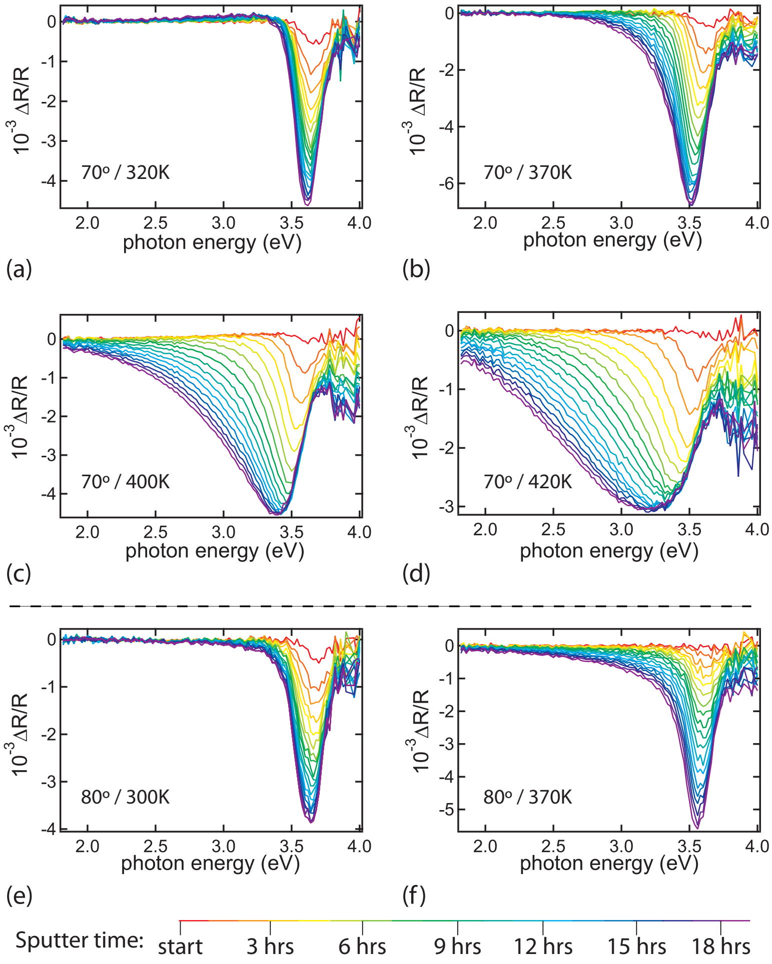

Figure 4.2: RAS spectra for different sample temperatures and angles of incidence. All samples were bombarded with 2000eV $Ar^+$ ions. For (a) - (d): $\theta_i = 70°$, ion current $j_i = 5\mu A\ cm^{-2}$ and sample temperatures 320K, 370K, 400K and 420K respectively. For (e) and (f): $\theta_i = 80°$, ion current $j_i = 2\mu A\ cm^{-2}$ and sample temperatures 300K and 370K respectively.

Annealing experiments have alse been carried out after the sputter experiments, to check the stability of the structures. Without changing the temperature, the change in the RAS spectrum has been monitored after the ion beam has been switched off. After one hour, a decrease of about 3% of the RAS signal has been found for a sample temperature of 350K. For a sample temperature of 420K, a decrease of 20% has been found. For both temperatures no redshift of the feature has been observed, which indicates that the ripple periodicity remains the same at the time scale of the experiment. Since an optical scan takes about 18 minutes, an error of only a few percents in the RAS signal occurs within one spectrum. The cooling down of the sample to 130K after switching off the ion beam only takes a few minutes. The annealing effect during this cooling down is therefore negligible in all cases discussed here.

In figures 4.2e and 4.2f, the evolution of the RAS spectra during ion bombardment at a polar angle of $\theta_i = 80°$ is shown for two temperatures. The energy position of the features is close to the surface plasmon energy. The average periodicity must therefore be around or below 200nm. Because of this small ripple periodicity at 80° incidence, it is not possible to determine the shift in periodicity as a function of temperature and sputter time. The full analysis of the optical spectra is therefore limited to the data taken at $\theta_i = 70°$.

High resolution LEED measurements reveal that the structures by ion bombardment show well defined facets as has also been observed for Cu(001) [42]. It is not possible to distinguish whether the structures are pits or hillocks with these diffraction measurements. In our analysis we assume dealing with pits. In figure 4.3, the LEED measurements are shown after sputtering at polar angles of incidence of 70° and 80°. The image after ion bombardment at a polar angle of incidence of $\theta_i = 70°$ has been recorded at a slightly out-of-phase diffraction condition with $S_{[001]} \approx 4.9$. Note that the perpendicular momentum change $q_{[001]}$ is represented by the phase $S_{[001]}$ relating to $q_{[001]}$ by $q_{[001]} = S_{[001]}\,(2\pi/d)$ with d representing the interlayer spacing. Six intensity maxima are identified, three spots at the illuminated side (IR, IL and I) and three spots at the shadow side (SR, SL, S). The pattern exhibits mirror plane symmetry with the mirror plane defined by the plane of incidence of the ion beam. The distance of the intensity maxima with respect to the position of the specular beam ($q_{[110]} = q_{[\bar{1}10]} = 0$) increases with increasing $\Delta S = \mathrm{int}(S) - S$, indicating that they arise from facets. This similar diffraction pattern is observed after all erosion experiments, independent of the substrate temperature. At $\theta_i = 80°$, the pattern reduces strictly to only intensity distributed in the plane perpendicular to the plane of incidence of the ion beam, indicating a 1D ripple pattern. Besides the Bragg peak, only two intensity maxima are identified (R and L) in this case. The length of the ripples is then beyond the resolution of the instrument used, i.e. at least 100 nm. The pattern is again similar for all sample temperatures.

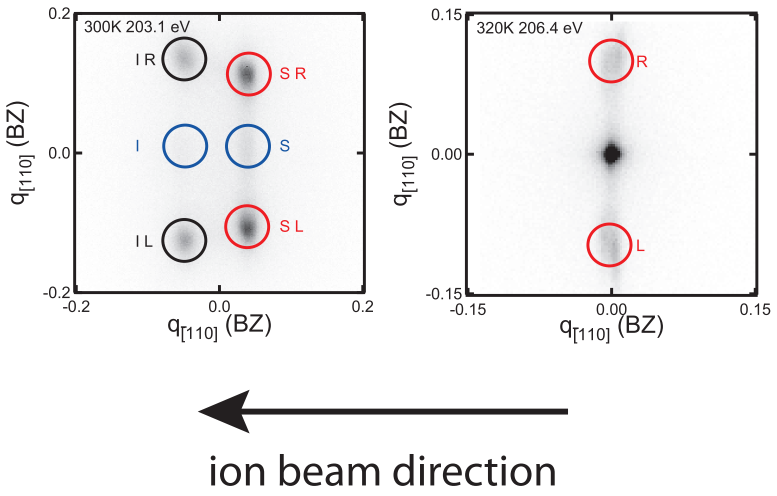

Figure 4.3: Typical HR-LEED patterns after prolonged sputtering. Both patterns have been obtained under slightly out of phase conditions ($S_{[001]} = 4.9$; see text). The ion beam was incident from the right. Assuming to deal with pits, the diffraction peaks are identified as resulting from shadow-side (S) - and illuminated (I) facets and from left (L) - and right hand side (R) facets. At a polar angle of 70° (left hand panel) the pattern is 3D (2D in the (001)-surface plane), while at 80° (right hand panel) the pattern is 2D (1D in the (001) surface plane).

In figure 4.4a the positions of the four most pronounced diffraction spots (SR, SL, IR and IL) are shown as a function of the normalized perpendicular phase $S_{[001]}$ for the 70° case. Towards the in-phase condition ($S_{[001]} = 5.0$) the spots move all to the center. This is the position of the $(0, 0)$ (Bragg) spot, which is only visible close to the in-phase condition. The small width of the Bragg peak upon varying the perpendicular phase indicates that the structures are at least several layers deep [48, 49]. For increasing $\Delta S$, two weaker side peaks (S and I) appear allong the high symmetry ($q_{[110]}$ and $q_{[\bar{1}10]}$) directions. These peaks indicate smaller, less pronounced facets. The orientation of all facets is determined from the displacement of these peaks as function of the perpendicular phases. We find that the displacement in the plane parallel to the surface is slightly different for the facets on the

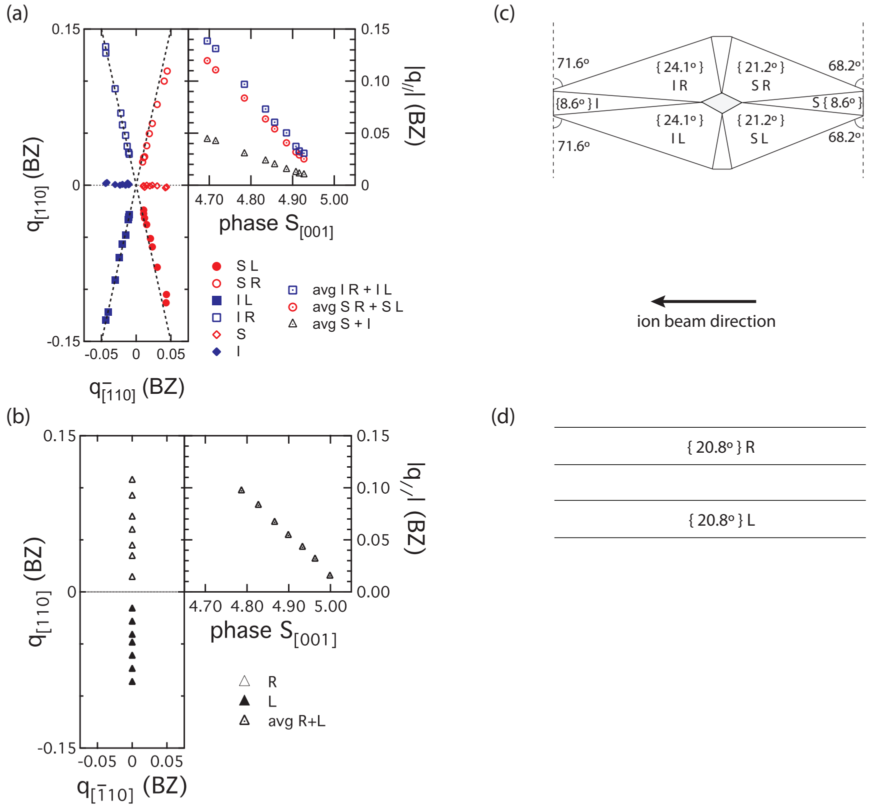

Figure 4.4: Elucidation of typical majority features on Ag(001) after prolonged bombardment at grazing incidence as revealed by HR-LEED patterns (cf. Fig. 3). Left hand panels in (a) and (b): Facet peak positions as a function of the changes, q, in electron wave vectors along the $[\bar{1}10]$ and the [110] azimuth for various electron energies between 203.1 and 223.2 eV. Right hand panels of (a) and (b): The average parallel components of the electron wave vector change for the various facets vs the vertical scattering phase $S_{[001]}$ (see text). The surface component of the ions is parallel to $[\bar{1}10]$ in all cases. The polar angles of incidence are 70° (a) and 80° (b), with ion fluences $5\mu A/cm^2$ and $2\mu A/cm^2$, respectively and surface temperatures of 300K and 320K, respectively. The corresponding schematic surface features are shown for 70° in (c) and for 80° in (d). Assuming as before etch pits the symbols I and S refer to facets on the illuminated and the shadow sides, while L, and R refer to left hand and right hand as seen by the incident ions.

illuminated and shadow side of the erosion pit. The spots on illuminated side (IR and IL) have an angle of 71.6° with the high symmetry $[\bar{1}10]$ direction. This corresponds to stepedges in this facet with a [130] orientation. The angle of the spots on shadow side (SR and SL) have an angle of 68.2° with respect to the high symmetry $[\bar{1}10]$ direction. This corresponds to a [250] direction of the step edges in this facet. The diffraction features on the shadow side have a significantly stronger intensity. The facet on the incident side of the etch structure has better developed. This is probably the result of the local incidence angle of the ion beam on the facets on the shadow side, which is below 15° with the local interface. The local incidence angle is than below the critical angle for sputtering [50] . Below the critical angle, the sputter yield decreases dramatically as most ions are reflected from the surface without an energy transfer impact. However, any protrusion on these facets are very likely to be sputtered away by the ion that skims over the surface for a local incidence angle below the critical angle [51]. A very efficient mechanism for the creation of well defined facets is thus obtained. In figure 4.4b the positions of the diffraction spots are shown as a function of the normalized perpendicular phase $S_{[001]}$ for the 80° case. The pattern is in this case one dimensional and only two facets are present. The diffraction spots move along the high symmetry [110] direction, indicating that the facets are orientated along the sputter direction.

On the right side of figures 4.4a and 4.4b, the parallel displacement ($|q_{//}| = \sqrt{q^2_{[110]} + q^2_{[\bar{1}10]}}$) of the facet peaks with respect to the origin is plotted as function of the phase $S_{[001]}$. In the 70° case, a different facet angle has been found for the facets on the illuminated and shadow side of the erosion pit. A facet angle of 21.2° is found for the shadow facets (SR, SL) and a facet angle of 24.1° is found for the illuminated facets (IR, IL). Also shown are the displacements with perpendicular phase of the less pronounced side peaks (I, S). They reveal facets with an angle of 8.6° with the surface. After sputtering at a polar angle of 80°, the facet angles of the ripple walls are 20.8° (R, L). Figure 4.4c and 4.4d summarize these angles and show the contours of the avarage ion erosion pit for both cases.

## 4.4 Quantitative analysis of the optical spectra

The Rayleigh-Rice Theory (RRT) has extensively been used to quantify surface roughness as measured with ellipsometry, see ref. [52] and references therein. This approach is applicable for relatively small variations on the surface, i.e. $\sigma/\lambda \overset{<}{\approx} 0.05$ and $\sigma/L \overset{<}{\approx} 0.3$, where $\sigma$ is the root mean square (rms) roughness of the surface, $\lambda$ is the wavelength of the incident light and $L$ is the characteristic length scale of the surface roughness. The measured surface roughness in our experiments is of the order of a nanometer, and is well within the limits for using the RRT-analysis.

The RRT is a perturbation approach for the solution of the Maxwell equations on rough surfaces and has been extensively described by Ohlídahl and coworkers [52] and is given in eq. 4.2. The zeroth order term ($\hat{r}_j^{(0)}$) is the Fresnel reflection coefficient for reflection on a smooth surface, with polarization j. The perturbation term consists of the convolution between the optical response function $\hat{f}_j(K_{[\bar{1}10]}, K_{[110]}, k_0)$ and the normalized power spectral density function (NPSDF) $w(K_{[\bar{1}10]} - k_0 \sin(\theta_0), K_{[110]})$, where $k_0$ is the wave vector of the incident light at a polar incidence angle of $\theta_0$ and $K_{[\bar{1}10]}$ and $K_{[110]}$ are the reciprocal lattice vectors parallel to the surface, which are used to describe the periodicity of the roughness in reciprocal space.

$$\begin{aligned}\hat{r}_j = \hat{r}_j^{(0)} + \sigma^2 \int_{-\infty}^{+\infty} \int_{-\infty}^{+\infty} & \hat{f}_j(K_{[\bar{1}10]}, K_{[110]}, k_0) \times \\ & w(K_{[\bar{1}10]} - n_0 k_0 \sin(\theta_0), K_{[110]}) dK_{[\bar{1}10]} dK_{[110]} \end{aligned} \qquad (4.2)$$

The rather complex optical response function $\hat{f}$ is simplified by measuring at (near) normal incidence ($\theta_0 \approx 0$). The surface structures are further considered to be one-dimensional. This reduces the K-vector along the ion beam direction to zero and thus integration over $K_{[110]}$ vanishes. Under these circumstances the anisotropic optical reflection can be described by eq. 4.3, where $\epsilon$ is the complex dielectric function of silver. The representation of the NPSDF by a single Gaussian function is found to provide a sufficient description of the data. The use of multiple Gaussians did not result in a significantly better fit. This implies that the pattern at 70° behaves optically as a 1D structure with negligible change in optical response parallel to the ripples. For the Gaussian distribution the mean value represents the average periodicity of the pattern while the width represents the spread in this periodicity.

$$\begin{aligned}\frac{\Delta r}{r} &= \sigma^2 \int_0^{\infty} -2K_{[\bar{1}10]} k_0 \left( \frac{\sqrt{\kappa - 1} - \sqrt{\kappa\epsilon - 1}}{1 + \sqrt{\kappa - 1}\sqrt{\kappa\epsilon - 1}} \right) \\ &\quad \times w(K_{[\bar{1}10]}) dK_{[\bar{1}10]} \\ \kappa &= \left( \frac{k_0}{K_{[\bar{1}10]}} \right)^2 \end{aligned} \qquad (4.3)$$

Figure 4.5 shows two typical measurements and the fitted spectra. All measured spectra can be described with similar accuracy. Note that for an average periodicity below 200 nm, the plasmon feature remains at the position of the surface plasmon on the silver surface. The RAS technique cannot yield the periodicity although the roughness can be established. The corresponding NPSDF's that are the result of the fit are also shown. We find a considerable broadening of the ripple periodicity with increasing period. The observation of plasmonic features on the Ag surface enables already a direct link between the peak position and the ripple periodicity via the dispersion relation of silver [24]. The maximum position found for the PSDF fitted to the reflection difference spectra confirms this relation.

The evolution of ripple periodicity and roughness with sputter time is shown in Fig. 4.6. In these graphs, only the results for a 70° polar angle of incidence of the ion beam for the highest substrate temperatures is shown. Only under these conditions, the plasmon features are observed at a position that differs from that of the surface plasmon and the periodicity of the ripple pattern can be determined. The increase with time of the ripple periodicity in the first 300 min. is very different from the later stage. The time of the crossover point decreases with increasing temperature. No saturation of neither the average ripple periodicity nor the surface roughness is observed.

## 4.5 Discussion

Ion bombardment at polar angles of incidence of 70° or 80° results in the creation of different structures as indicated by LEED. The most grazing

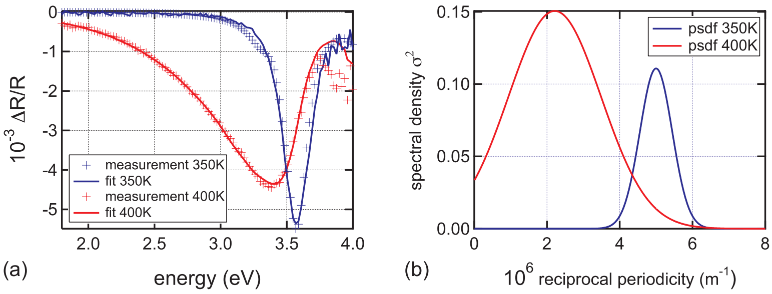

Figure 4.5: (a) The measured reflectance difference spectra data is indicated with markers. Data is obtained after 18 hours of sputtering with an polar angle of incidence of the ion beam of $\theta_i = 70°$ and sample temperatures of 350K and 400K. The modeled data is indicated with solid lines and based on a Gaussian distributed PSDF. (b) Gaussian shaped power spectral density functions, used to obtain the modeled spectra in (a).

incidence situation (80°) results in the creation of 1D nanogrooves as has already been reported by van Dijken et al. on the Cu(001) surface [35]. The intensity of the RAS spectra increases with fluence, indicating that the height of the grooves increases with time in contrast to the lower ion energy results for Cu(001). The LEED measurements of the deeper grooves on the Ag(001) surface created by 2keV $Ar^+$ ions show that these grooves indeed have a rectangular profile perpendicular to the ripple direction. The high and low region of the grooves are connected by an edge that consists of a {113} facet. At a polar angle of incidence of 70° the LEED measurements show a limited lateral size of the created structure, i.e. a more 2D character with an elongated diamond surface pattern. The optical data can, however still be described well by a 1D optical anisotropy. No sufficient redshift of the plasmon features was noted for sputtering at a substrate temperature below 400K. This limits the applicability of the RAS method for quantitative

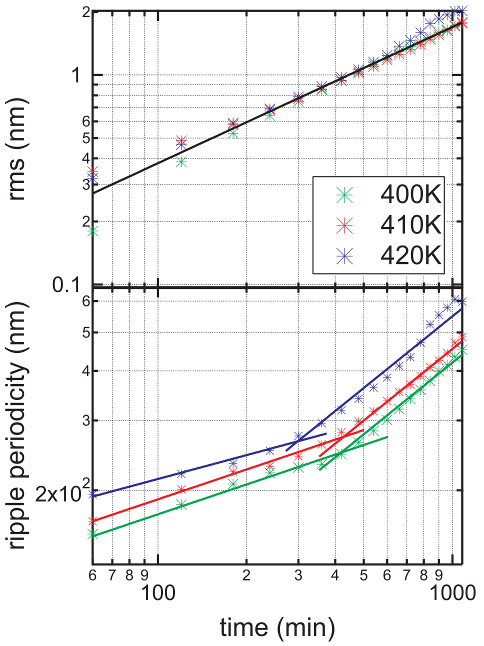

Figure 4.6: The development of surface rms (top) and the ripple periodicity (bottom) during sputtering as function of time for different sample temperatures. The values have been calculated with the RRT fitting procedure described in the text. The solid lines indicate in the top graph the slope with exponent $\beta$ and in the bottom graph the slope with exponents $p$.

analysis under these experimental conditions.

Chan and Chason reported a kinetic phase diagram for pattern formation on Cu(001) and Ag(001) surfaces through ion erosion at a polar angle of incidence of 70° [14]. As a function of ion current and temperature various regions are identified. At low temperatures, the effectiveness of various interlayer mass transport channels is determined by the associated Ehrlich Schwoebel (ES) barriers. The specific values of these barriers explain the pattern formation on the surface. This is therefore called the ES instability region. At more elevated temperature, the ion flux determines whether roughening is observed. For low flux no roughening is observed while for higher ion flux the pattern formation can be described by the Bradley Harper (BH) approach, the BH instability region. The results of this work are related to the ES instability region. However, on the basis of the kinetic phase diagram mentioned, the experiments should at least cover two of the regions, as a non-roughening situation is predicted above 380K. Valbusa et al [8] indeed observed rather isotropic structures after 20 min. of 1keV $\mathrm{Ne}^+$ ion erosion at 400K with an ion current $j_i = 2.2\mu\mathrm{A\ cm}^{-2}$. However, in the experiments presented in the present work, anisotropic nanopatterns are observed at temperatures as high as 420K. This is probably due to the 50 times longer sputtering with 2keV $\mathrm{Ar}^+$ ions and the higher ion current of $j_i = 5\mu\mathrm{A\ cm}^{-2}$. After 20 min. sputtering we also note only a slight anisotropic nanopattern. This shows that not only ion flux and temperature, but also the fluence is an important parameter for the kinetic phase diagram. The high resolution LEED images indicate that, we do not have elongated ripples as predicted by the Bradley Harper theory. The etch pits show a rather strongly elongated diamond shape. This would imply that these structures fall in the category of nanopatterns that are the result of ES instabilities. The Ehrlich Schwoebel (ES) barrier of the $\langle 110 \rangle$ step edges reduces the path way of interlayer mass transport across these step edges [53]. Interlayer mass transport via kink positions in the $\langle 110 \rangle$ step edge is strongly favoured for the Cu and Ag (001) surface [7,42,54]. This explains the observation of the elongated diamond shape as this induces a large number of kinks. For higher ion currents, a transfer to the BH instability region with the observation of 1D ripples for a polar angle of incidence of 70° is expected, in line with reported ripple pattern formation on the Cu(001) surface [25].

For elevated temperatures the increase of both periodicity and roughness with time was determined. After an initial period with only a small increase in periodicity, a transition to a stronger increase with fluence is found. However, no saturation of the periodicity has been found, i.e. we obtain no evidence for a stationary situation as described by the Bradley

Harper theory [6]. Recently, Cuerno and coworkers have extended the continuum description of ion erosion processes substantially [55]. The Bradley Harper theory and the more elaborate (anisotropic) Kuramoto-Sivashinsky theory are limiting cases of this description. Also this description allows to characterize the evolution of the ion induced nanopattern with scaling parameters that describe the change in periodicity and roughness with sputter time [56, 57]. The increase in roughness $\sigma$ with sputter time follows $\sigma \sim t^{\beta}$. The critical exponent $\beta$ has a value of $\approx 0.55$ for the experiments depicted in fig. 4.6. The change in periodicity $L$ is characterized by a critical exponent $p$, with $L \sim t^{p}$. Considering this critical exponent, two stages are identified in our experiments. The transition from the first stage to the second stage is temperature dependent and occurs earlier for higher temperatures. In the initial stage this critical exponent $p$ has a value between 0.2 and 0.25. These values are similar to the value of around 0.2 found from experiment and theory beyond the Kuramoto-Sivashinsky model [13, 43, 55]. However, in the second stage a value for critical exponent $p$ between 0.5 and 0.6 is found. The similarity of $\beta$ and $p$ in this regime indicate that the ratio of height and width of the ripple structures is about constant, independent of fluence and temperature. A value around 0.5 has been reported by Habenicht et al. [44] for the evolution of the periodicity of ripples created on Si(001). The evolution of these latter structures has been monitored in situ with SEM enabling to probe not only the periodicity but also the ripple propagation velocity. Also for this experiment, no saturation of the ripple periodicity is observed. This absence of saturation has been explained by the absence of nonlinear terms in the continuum description that would result in a ripple period that grows indefinitely with $p = 0.5$ [55, 58]. A similar exponent for the increase in roughness and period is also reported in these simulations. The higher value observed in our experiments might be associated to an efficient coarsening mechanism [55], as can be expected for the highly mobile species at temperatures around 400K.

## 4.6 Summary

Optical reflection anisotropy is a very suitable tool for the in-situ characterization of ion beam induced anisotropic periodic nanopatterns. With the Rayleigh Rice approximation, the optical response can be quantitatively interpreted in terms of the ripple period, rms and ordering. Also below the diffraction limit, the formation of a ripple pattern can be observed, albeight the ripple period can not be established. This limits the quantitative application for the measurement of ripple periods on Ag to structures with a characteristic length scale of at least 200nm. High resolution LEED data compliments the optical anisotropy observations. For a polar angle of incidence of 80° a 1D ripple nanopattern is obtained, while sputtering at 70° results in anisotropic features, which still have some persistent 2D character. The average shape of the ion pits created can be determined; they have a rather elongated, slightly distorted shape. For the description of the optical response, only the short distance between the etch pits has to be taken into account. A 1D model suffices. Also for extended sputtering time up to 18 hours (fluence $1.9 \times 10^{18}$ ions/cm$^2$), we do neither observe saturation behaviour of the ripple period at temperatures around 400K, nor a saturation of the rms roughness. This indicates that non-linear mechanisms that are usually observed in ion erosion are not present and coarsening still proceeds in an efficient manner.

# CHAPTER 5

## Evolution of the anisotropy of ion induced nanopatterns on Ag(001) determined with Reflection Anisotropy Spectroscopy

Reflection anisotropy spectroscopy (RAS) is used as an in-situ probe for the emergence and evolution of surface patterns on Ag(001) during oblique incidence ion bombardment. The information is extracted from plasmon resonances induced by the nanoscale patterns, utilizing the fact that smooth Ag(001) is optically isotropic. The Rayleigh Rice perturbation approach delivers the temporal development of the average periodicity and amplitude of the surface patterns. For ion bombardment at a polar angle of incidence of 70° along a $\langle 110 \rangle$ azimuth strongly anisotropic surface features develop, giving rise to a single plasmon resonance, which is described well with a one-dimensional power spectral density function. For a smaller polar angle of incidence of 61.5° multiple plasmon resonances are observed, which demand a two-dimensional power spectral density function for a perfect description. These result compare well with high-resolution low energy electron diffraction data, taken after ion bombardment at both angles of incidence. The optical data, obtained at 61.5° show coarsening and seem to suggest scaling of the periodicity and roughness, with critical exponents 0.27 and 0.40 respectively.

# 5. Evolution of the anisotropy of ion induced nanopatterns on Ag(001) determined with Reflection Anisotropy Spectroscopy

## 5.1 Introduction

Ion bombardment of surfaces can be used to both smoothen and roughen surfaces. The bombardment process can be such that an erosion instability is induced, leading to the formation of a variety of nanopatterns including ripples and dots [4, 8, 39, 41, 42]. The key parameter to characterise the nanopattern is its average lateral periodicity. Also the height variation, or roughness, and the distribution of the lateral periodicity are important quantities that characterize the nanopattern. The temporal evolution of these statistical quantities is an essential ingredient for understanding the mechanisms involved in the selforganisation process [57]. This temporal evolution is most effectively studied with techniques that can be employed in-situ. Both X-ray scattering [16] and light scattering [59, 60] have been used to characterize in-situ the evolution of ion induced ripple patterns. However, not only the scattered beam, but also a specularly reflected light beam contains a wealth of information about the periodicity and shape of structures. We demonstrated this by monitoring the evolution of ripple patterns created by means of glancing incidence ion bombardment of a Ag(001) surface via the variation of the specular optical reflection [33]. The coupling between the periodicity of structures and the resonance energy of generated surface plasmons enables a quantitative analysis [61]. The cubic symmetry of the Ag(001) gives rise to an isotropic optical response. An anisotropic pattern that evolves during oblique incidence ion sputtering results in an easily identifiable anisotropic optical response. This optical anisotropy can be measured with Reflection Anisotropy Spectroscopy (RAS). This technique involves a normalized optical bridge set-up that allows a sensitive measurement of the difference in reflectivity $r$ along two orthogonal directions ($r_\perp$ and $r_\parallel$) on the surface [19]:

$$\frac{\Delta r}{r} = 2\frac{r_\perp - r_\parallel}{r_\perp + r_\parallel} \tag{5.1}$$

The high sensitivity of RAS for recording optical anisotropy has led to its use to monitor semiconductor growth [62], to probe surface electronic states [63], to measure morphological surface structures (i.e. steps and islands) [17] and to determine the orientation and crystalline properties of adsorbed organic molecules [20]. The virtue of RAS in the study of nanopattern evolution during ion bombardment is that all isotropic contributions are suppressed. The focus is on the anisotropic contribution, i.e. the periodicity and the modulation height of the ion induced anisotropic pattern. The sign of the anisotropy signal already reveals the direction along which the periodicity evolves. For ripple structures, the spectra will only show plasmon induced features features with the same sign. In this paper we report on the observation of novel features with opposite sign in the optical anisotropy spectra. These features reflect the organisation of etch pit structures not only perpendicular to, but also parallel to the plane of incidence of the ion beam. The average shapes of the etch pit structures are elucidated from electron diffraction.

## 5.2 Experimental details

The experimental data were obtained during ion beam erosion experiments performed on a single crystalline Ag(001) sample in a UHV system. The sample was cleaned with multiple ion bombardment and anneal cycles. For the RAS measurements, a home-built system was used [33], the performance of which is analogous to instruments described in literature [19, 62]. The measurements described in this paper reflect the real part of the optical anisotropy given in eq. 5.1. The photomultiplier amplification was regulated to provide a constant DC reflectivity signal. This regulated photomultiplier voltage is used in the fit procedures as a measure of the accuracy of the experimental data. The light is incident along the normal of the surface. The parallel polarization direction in the optical experiments is aligned with respect to the plane of incidence of the ion beam. The measured anisotropy is the normalized difference between the two directions parallel and perpendicular to the plane of incidence of the ion beam. High resolution low energy electron diffraction measurements with an Omicron SPA-LEED instrument were used to characterize the average morphology of the periodic structures on the surface.

## 5.3 Anisotropic optical response of nanostructured surfaces

The Rayleigh Rice perturbation approach allows to relate the influence of roughness on the optical reflectivity of an interface. This approach was used by Kretschmann and Kröger to explain the observation of a surface plasmon resonance on silver surfaces [61]. A generalized description of the relation between roughness and interface reflectivity was provided by Franta and Ohlidal [52]. The perturbation approach of the solution of the Maxwell equations for a sharp interface expresses the change of the reflectivity as:

$$\hat{r}_{\perp,\parallel} = \hat{r}^{(0)}_{\perp,\parallel} + \sigma^2 \int_{-\infty}^{\infty} \int_{-\infty}^{\infty} \hat{f}_{\perp,\parallel}(\vec{K}, k_0) \times w(\vec{K}) d\vec{K} \tag{5.2}$$

where $\hat{r}^{(0)}_{\perp,\parallel}$ is the reflectivity of the unperturbed surface. The surface roughness is quantified by the rms roughness $\sigma$ and the normalized Power Spectral Density Function (PSDF) $w(\vec{K})$. This spatial information is spanned by the spatial wave vector $\vec{K}$ on the surface. The interaction with the light is provided by the kernel $\hat{f}$, which depends on the wave vector of the incident light $k_0$ and the reciprocal length $\vec{K}$. For normal incidence, the kernel $\hat{f}_\perp$ can be written as:

$$\hat{f}_\perp(K_\parallel) \quad = \quad -2k_0 \hat{r}^{(0)}_\perp |\hat{K}| \left( \frac{k_0}{|\hat{K}|}\sqrt{\epsilon} + \frac{(\hat{b}-\hat{c})\left(\left(\frac{K_\parallel}{K}\right)^2 + \hat{b}\hat{c}\right)}{1+\hat{b}\hat{c}} \right) \tag{5.3}$$

with $\hat{b}, \hat{c}$ and $K$ defined as:

$$\begin{aligned} \hat{b} &= \sqrt{\left(\frac{k_0}{K}\right)^2 - 1} \\ \hat{c} &= \sqrt{\left(\frac{k_0}{K}\right)^2 \cdot \epsilon - 1} \\ K &= \sqrt{K_\perp^2 + K_\parallel^2} = \left|\vec{K}\right| \end{aligned} \tag{5.4}$$

The dielectric constant of the reflecting material is expressed by $\epsilon$. For $\hat{f}_\parallel$ an analogous expression is found. Note that eq. 5.3 seems to indicate that the reflectivity in one direction depends only on the spatial wave vector in the orthogonal direction. This is trueonly at first glance, as the coefficients $\hat{b}$ and $\hat{c}$ also depend on the magnitude of the spatial wave vector.

With these definitions the reflectivity difference of an anisotropically rough surface on top of an optically isotropic substrate can be evaluated:

$$\begin{aligned} \frac{\Delta r}{r} &= 2 \cdot \frac{(r_\perp - r_\parallel)}{(r_\perp + r_\parallel)} \\ &= \frac{\sigma^2}{\hat{r}^{(0)}} \int_{-\infty}^{\infty} \int_{-\infty}^{\infty} (\hat{f_\perp} - \hat{f}_\parallel) w(\vec{K}) d\vec{(K)} \end{aligned} \tag{5.5}$$

where $\hat{r}^{(0)} = \frac{1}{2} \cdot (\hat{r}_{\perp}^{(0)} + \hat{r}_{\|}^{(0)})$. The difference in the kernel $\hat{f}$ reduces to:

$$\begin{aligned} \hat{f_{\perp}} - \hat{f}_{\|} &= -2k_0\hat{r}^{(0)}|\vec{K}| \cdot \frac{(\hat{b} - \hat{c}) \cdot \left(\left(\frac{K_{\|}}{K}\right)^2 - \left(\frac{K_{\perp}}{K}\right)^2\right)}{(1 + \hat{b}\hat{c})} \\ &= -2k_0\hat{r}^{(0)}|K|\frac{(\hat{b} - \hat{c})}{(1 + \hat{b}\hat{c})} \cdot \cos 2\phi \qquad (5.6) \end{aligned}$$

The angle $\phi$ represents the direction of $\vec{K}$ with respect to the parallel direction. The selection of only the anisotropic roughness contribution to the optical response is made by the $cos2\phi$ term.

## 5.4 RAS Measurements

Figures 5.1 a) and b) display the development of the RAS signal for sputtering with 2 keV $Ar^+$ ions at a polar angle of incidence of 70° along the [110] azimuth at a surface temperature of 350K and 300K, respectively. An ion current of $5\mu A/cm^2$ recorded for normal incidence sputtering was used. The top part shows the anisotropy spectrum as recorded at the end of the measurement. The high temperature measurement (fig. 5.1 a) ) shows that the evolution of the plasmon resonance is characterized by an increase of the resonance strength and strength combined with a red shift of the resonance energy with fluence. The negative sign of the RAS-feature indicates that the etch pits show a periodicity in the direction perpendicular to the plane of the incident ion beam. This periodicity reveals the evolution of ripple structures parallel to the plane of incidence [34, 35]. These spectra can be described well with a (semi) one-dimensional surface morphology modulation [33]. The observed red shift indicates that the length scale of the periodicity is just above 200 nm. Although the spectra recorded at 300K (fig. 5.1 b) ) look similar to those recorded at 350K, they also show a slight, broad positive feature around 3.0 - 3.5 eV, which can be distinguished after about 500 min of sputtering. The maximum of this positive feature is indicated with the black dashed line. It indicates that also a slight ordering of the individual etch pits in the direction parallel to the plan of incidence of the ion beam occurs. The resonance energy of the negative peak in the 300K measurement is at a slightly higher energy than in the 350K. This indicates that the periodicity of the main structure is smaller in the low temperature situation. This is the direct a result of the lesser diffusion of species at a

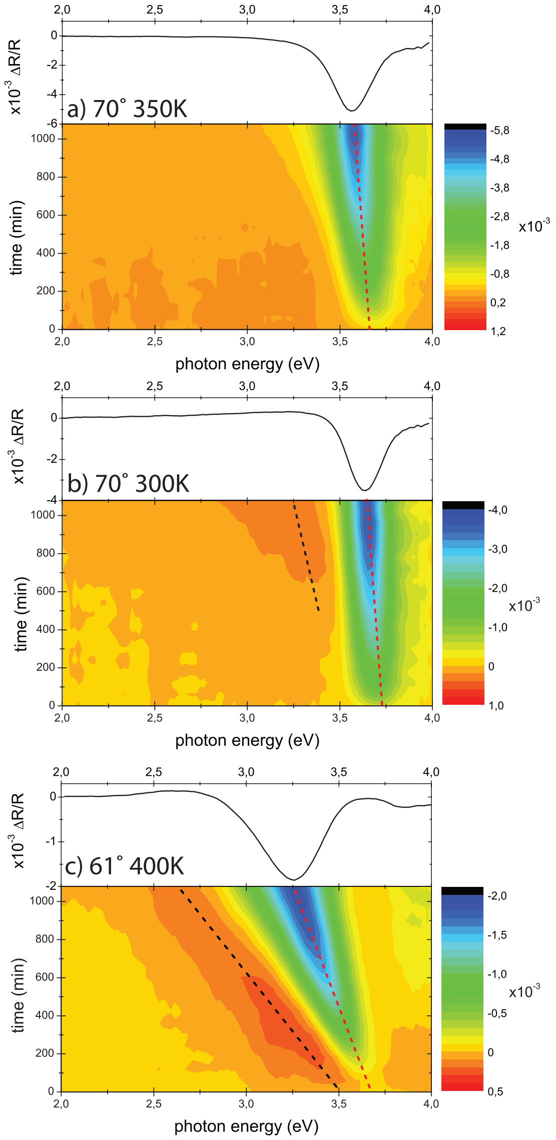

Figure 5.1: RAS measurement as a function of sputter time. The incident 2keV $Ar^+$ ion beam had an ion current of $5\mu A/cm^2$ at normal incidence. The images show three different temperature and polar angle of incidence conditions. a) 350K, 70° , b) 300K, 70° and c) 400K 61.5°. The red dashed line is a guide to the eye for the negative maximum, while the black dashed line is a guide to the eye for the observation of a positive maximum. The displayed spectra are the last spectra measured in the three time series.

lower temperature [34]. The positive resonance shows a considerably larger red shift with sputter time than the negative feature. Simulations show that this larger shift reflects the increased sensitivity for the characteristic length scale in this part of the spectrum [64].

The ordering of etch pits parallel to the plane of incidence of the ion beam as evidenced by the positive optical feature, can be influenced by the angle of incidence of the ion beam. Figure 5.1 c) shows the result for a polar angle of incidence of 61.5°. Note that this change in the polar angle of incidence also influences the ion flux; the flux at 61.5° is 40% higher than at 70°. The increased flux with decreasing polar angle of incidence would lead to an increased number of diffusing species on the surface. This would result in a decreased length scale. To compensate for this effect, the sample temperature is increased to 400K to assure sufficient diffusion on the surface and thus the emergence of a characteristic length scale above 200 nm. The displayed evolution shows two well pronounced features of opposite sign indicating the orientation of etch features with two distinctly different, orthogonally oriented, length scales. Both resonances show a distinct red shift revealing a considerable increase in average periodicity (coarsening) with sputter time.

## 5.5 LEED Measurements

To elucidate the average shape of the etch features, low energy electron diffraction images were taken after sputtering of the Ag(001) surface. Such images as displayed in fig. 5.2 show that markedly different structures evolve during sputtering at a polar angles of 70° and 61.5°. The images recorded for the more oblique incident angle were related to an etch pit with a top view of a slightly distorted rhombus shape and facets with an inclination angle around 23° [33]. This average etch pit structure was evaluated from the electron energy dependency of the four observed diffraction features. Variation of the electron energy and the corresponding position change of the diffraction feature are used to evaluate the normalized parallel ($\vec{q}$) and perpendicular scattering vector ($S_{[001]}$) [49]. The normalization is with respect to the reciprocal lattice vectors of Ag(001). The electron energy dependency of the four diffraction features recorded after sputtering at an angle of 61.5° is displayed in fig. 5.3. This image shows that the position of the diffraction features in the Brillouin Zone is electron energy dependent and move to a single spot for the in-phase condition ($S_{[001]} = 5$). This indicates that these diffraction features signify the presence of facets. The orientation of these

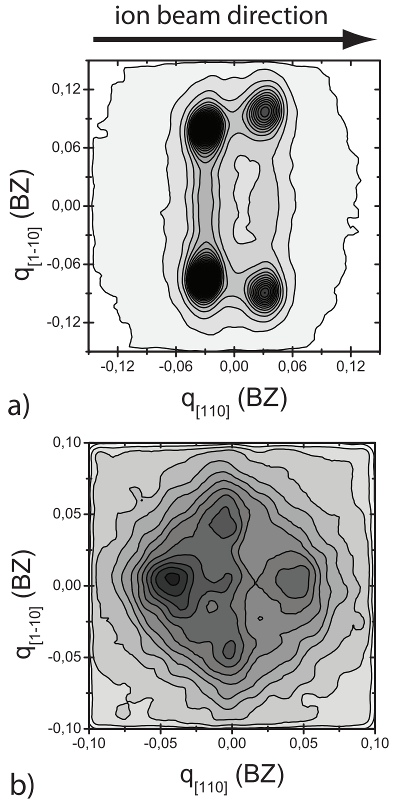

Figure 5.2: HR-LEED pattern measured after ion bombardment of the Ag(001) surface as displayed in fig.5.1 a) and c). a) polar angle 70° and temperature 350K. Measured at an electron energy of 210.7eV ($S_{[001]} = 4.806$) and b) polar angle 61.5° and 400K. Measured at an electron energy of 216.0eV ($S_{[001]}$=4.866)

facets is derived from the slope seen in the $S_{[001]} - \vec{q}$) plot (see e.g. reference [29] and reference therein). The facet on the illuminated side shows an inclination angle of 13.6°, while the others show an inclination angle of about 17°. These angles indicate facet orientations around [117] and [115], respectively. The intensity and the different angle on the illuminated side is explained by the local angle of incidence on this facet. For the polar angle of incidence used, the local angle of incidence is 15°, just around the critical sputter angle [50]. This leads to a different sputter condition, resulting in the altered illumination. From the combination of the RAS and LEED measurements, we conclude that the average shape of the etch pits is an inverse mound with rectangular base. The rectangular structure is retrieved from the RAS measurements that provides the periodicity in both directions.

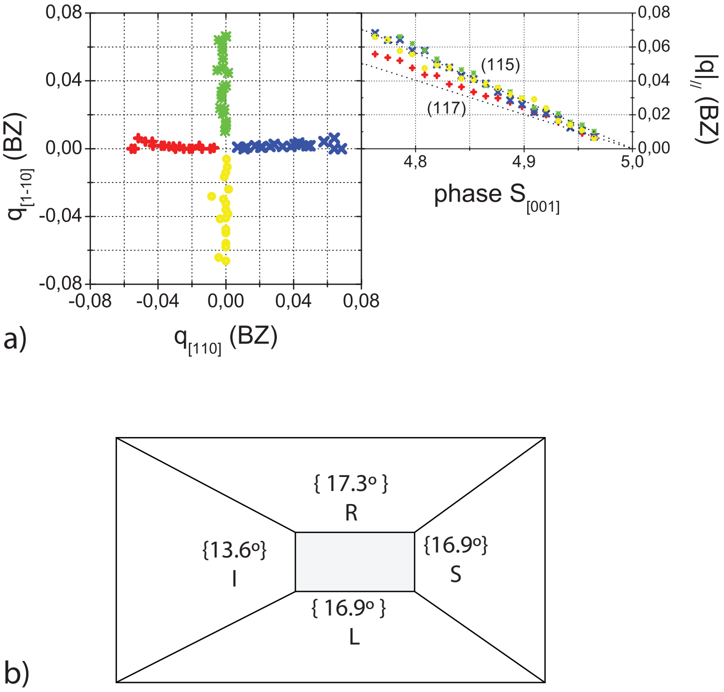

Figure 5.3: Position of the facet spots measured as a function of the electron energy for the pattern as displayed in Fig. 5.2 b). a) Left-hand panel: The four facet peak positions as a function of the parallel scattering vector of the electron beam, $\vec{q}_{//}$. The value of $\vec{q}_{//}$ in the $[1\bar{1}0]$ and $[110]$ azimuth is plotted for electron energies between 203.1 and 223.2 eV. Right-hand panel: The average parallel components of the scattering vector change for the various facets vs the vertical scattering phase $S_{[001]}$. The surface component of the ions is parallel to the $[1\bar{1}0]$. b) Sketch of the average etch pit shape with the 4 facet angles indicated. The ion beam is incident from the left. I indicates the illuminated facet and S indicates the shadowed facet. R and L indicate both right and left sides.

The very different diffraction patterns observed for sputtering at a polar angle of incidence of 70° and 61.5° were already indicative for the different average etch pits, i.e. a rhombus and an inverse rectangular mound respectively. Such a strong angular dependence was also observed for the very similar Cu(001) surface [34]. Two key factors strongly influence these structures. First of all the interlayer mass transport which is on this surface determined by the Ehrlich - Schwoebel barriers. These barriers are very different for the $< 110 >$ and $< 100 >$ step edges on this surface [30,34,37,53].

Secondly, the result of the ion impact shows a strong dependence on the crystal structure observed at angles of incidence near the critical angle for channeling [65].

## 5.6 Determination of roughness evolution

### 5.6.1 Gaussian roughness distribution

The RAS spectra recorded during ion beam sputtering at 70° shown in fig:5.1 a) show a strong feature with a negative sign. This signals an anisotropy with a periodicity in only one direction, perpendicular to the ions' plane of incidence. This roughness can be described well with a single 1D Gaussian PSDF [33]

$$w(\vec{K}) = \frac{\sigma^2}{\sqrt{2\pi}\delta} e^{-(\vec{K}-\vec{K}_0)^2/2\delta^2} \tag{5.7}$$

with $K_0$ the average reciprocal length, $\delta$ the width of the distribution and $\sigma$ the rms of the anisotropic part of the surface roughness. The actual PSDF characteristic for the roughness consists in this case of an azimuthally isotropic and an anisotropic component in the direction perpendicular to the ion beam. The RAS measurements are not sensitive to the first, and only the anisotropic part is probed. Different model functions for the anisotropic roughness distribution were investigated. The single Gaussian function characterized by three fit parameters ($\sigma$, $\delta$ and $\vec{K}_0$) gave the best representation of the measured data with a limited number of coefficients.

The RAS spectra obtained for an incident angle of the ion beam of 61.5° are more complicated. The positive and negative peaks reflect a significant deviation from the isotropic roughness PSDF in, respectively, both the perpendicular and parallel direction. This anisotropy was modelled with two Gaussians to represent the observed periodicity in both the parallel and perpendicular direction:

$$w(\vec{K}) = \frac{\sigma_\perp^2}{\sqrt{2\pi}\delta_\perp} e^{-\frac{(\vec{K}-K_{0,\perp})^2}{2\delta_\perp^2}} + \frac{\sigma_{//}^2}{\sqrt{2\pi}\delta_{//}} e^{-\frac{(\vec{K}-K_{0,//})^2}{2\delta_{//}^2}} \tag{5.8}$$

Figure 5.4 a) displays the anisotropic PSDF that was obtained from the fit to the RAS spectrum recorded following the ion bombardment. Both the positions $K_{0,\perp}$ and $K_{0,//}$, the strengths $\sigma_\perp$ and $\sigma_{//}$, and the width $\delta_\perp$ and $\delta_{//}$, of the two Gaussians were optimized.

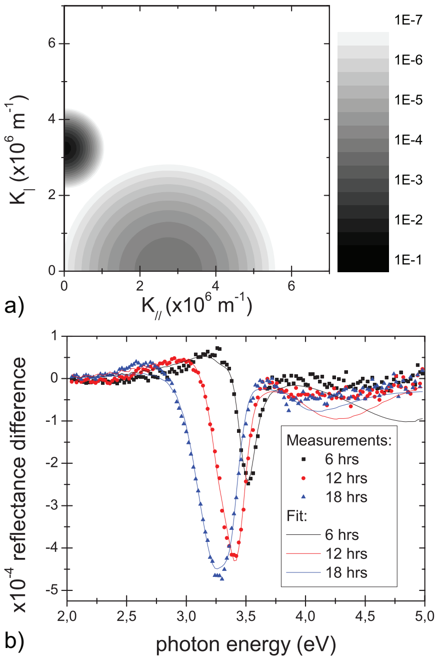

Figure 5.4: (a) Contour plot of the anisotropic PSDF obtained from a fit to the RAS spectrum recorded after 18h sputtering at a polar angle of 61.5°. (b) Measured and fitted results at 3 stages of the ion sputtering at a polar angle of 61.5°.

Figure 5.4(b) shows both the measured and fitted RAS spectra at three moments during sputtering; more specific: after 6,12 and 18 hours. Both the positive and negative features at various stages of the ion erosion process are well represented by the PSDF of eq. 5.8. The periodicity and strength obtained by fitting the spectra recorded during sputtering are displayed in Fig. 5.5. The temporal evolution of the strength shows a change in behaviour around 580 min. This change is not observed in the evolution of the periodicity in the perpendicular direction. Initially, the perpendicular periodicity is around 200 nm, and starts to increase after about 200 minutes. However, this is probably due to an experimental artefact. The shift in resonance energy for structures with a periodicity below 200 nm is very small. It is therefore likely that the periodicity is already increasing at an earlier stage. The periodicity in the parallel direction is initially around 310 nm and only slightly increasing in time. For the entire monitored time window, the periodicity in the parallel direction is well above the periodicity in perpendicular direction. After about 580 minutes a change in the strength evolution is noted. In the perpendicular direction a saturation is observed, while the periodicity still increases. In the parallel direction the strength even decreases for prolonged sputtering. This signifies that the ordering in this direction becomes smaller and might point to that the surface features become more one dimensional in this stage.

The evolution of the average periodicity and the strength are often characterized by a critical exponent [57]. The increase of the average periodicity $L$ in the perpendicular direction could be characterized with a critical exponent n=0.27, with $L \propto t^n$. The initial increase of the strength in both directions can be characterized by an exponent $\beta$, with $\sigma \propto t^\beta$. For both the perpendicular and parallel directions an almost similar value for $\beta$ is found, $0.40 \pm 0.01$. Note however, that in both the periodicity and roughness the exponents only describe the behaviour for a limited time window.

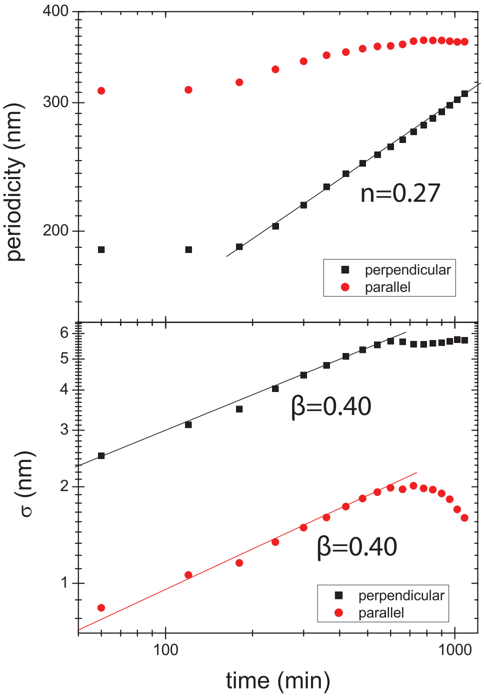

Figure 5.5: Fit parameters of the RAS spectra obtained during sputtering at a polar angle of incidence of $\theta_i = 61.5°$. (left) time evolution of the strength of the two Gaussian functions. (right) time evolution of the average length scale in the two perpendicular directions.

### 5.6.2 Roughness evolution via EW model with Mullins diffusion

Bradley and Harper discussed the pattern formation as a result of an erosion instability with an analysis of a continuous description of the erosion process [4]. Several more detailed models have been developed, considering the details of the sputtering and diffusion processes [6]. An analytical solution for the evolution of the surface height is with these often non-linear models not possible. An analytical expression with a limited applicability for the development of the PSDF is possible with the extended Edwards-Wilkinson (EW) model [56]. The rate equation for this model is given by eq. 5.9. The EW model assumes that the growth is given by a random roughening of the surface, given by $\eta$ and an additional roughening by a surface tension term due to the ES-barrier, proportional to $\nu$.

$$\frac{\delta h}{\delta t} = \nu \nabla^2 h + \eta \tag{5.9}$$

To make the EW-model applicable for a description of our experiments, a diffusion term $\kappa \nabla^4 h$ was added to enable smoothening. This term is similar to diffusion term used in the the Mullins diffusion equation [5, 56]:

$$\frac{\delta h}{\delta t} = \nu \nabla^2 h + \kappa \nabla^4 h + \eta \tag{5.10}$$

The sign of $\kappa$ and $\nu$ are opposite, since the diffusion counteracts the erosion effect. The analytical solution for the time evolution of the PSDF with an anisotropic erosion and diffusion process can be obtained [57]:

$$P(k_x, k_y) = \frac{1 - exp(-2t \cdot (\nu_x \cdot k_x^2 + \nu_y \cdot k_y^2 + \kappa_x \cdot k_x^4 + \kappa_y \cdot k_y^4 + \kappa_{xy} \cdot k_x^2 k_y^2))}{\nu_x \cdot k_x^2 + \nu_y \cdot k_y^2 + \kappa_x \cdot k_x^4 + \kappa_y \cdot k_y^4 + \kappa_{xy} * k_x^2 k_y^2} \tag{5.11}$$

This PSDF shows a typical elliptical shape. The parallel and perpendicular radius of this ellipse represent the correlation lengths on the surface. Figure 5.6 shows the fit of this PSDF to 3 typical spectra as well as the optimal PSDF for the largest erosion time. Note that maxima are at different location than for gaussian. The fit is slightly worse than was possible with the two gaussian functions. This is especially noted around the maximum of the peak after 6 and 12 hrs. sputtering. The PSDF of eq. 5.11 has two correlation lengths that are strongly coupled. The fit is thus much more sensitive to slight variations resulting in a less accurate representation in the positive part of the spectrum. Another consequence is a strong coupling of the fit parameters. Components along the diagonal are minimal, since RAS is not sensitive for these parts. The obtained PSDF shows clear maxima in the two perpendicular directions signifying the two periodicities.

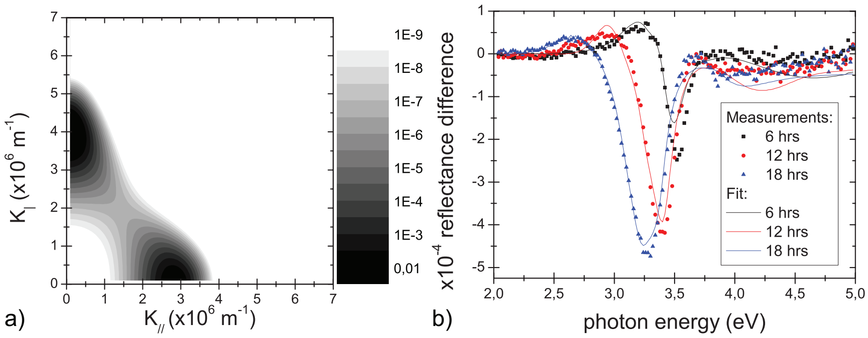

Figure 5.6: (a) Power spectral density function as derived from EW-model with Mullins diffusion and fitted with the experimental optical data (b) Comparison between the measured spectra and the spectra calculated with the PSDF of (a).

## 5.7 Conclusion

The optical reflection anisotropy as measured with RAS was used to characterize in-situ the evolution of the self-organisation during oblique incidence ion sputtering of Ag(001). A quantitative analysis of the optical spectra is possible with the Rayleigh Rice perturbation approach. In this description, the spectra are well represented by two Gaussians representing the anisotropic roughness parallel and perpendicular to the plane of incidence. The temporal evolution of the average periodicity and the roughness amplitude show that the average periodicity between etch features is always larger parallel to the ion beam. Both components grow in a similar way, but after saturation of the anisotropic roughness, the ordering along the beam directions starts to decrease. The combination with LEED measurements show that the induced nanopatterns consist of inverse mounts with a rectangular base.

# CHAPTER 6

## Plasmon resonance shift during grazing incidence ion sputtering on Ag(001)

Grazing incidence ion sputtering was used to create shallow ripple patterns on a Ag(001) surface. The anisotropic plasmon resonance associated with this ripple pattern can be sensitively measured with Reflection Anisotropy Spectroscopy. A slight red shift of the resonance energy is observed with increasing ion fluence. The observed resonance feature is described well with a skewed Lorentzian line shape. This line shape is the small roughness length scale limit of the Rayleigh Rice perturbation approach. The width of this line shape is directly related to imaginary part of the dielectric function, which shows a roughness induced reduction of the electron mean free path. The observed change in resonance energy and strength with ion fluence is discussed.

## 6.1 Introduction

Ion beam sputtering is a well established technique for the creation of a ripple pattern on a wide variety of surfaces. These patterns are the result of a balance between heterogeneous ion sputtering and diffusion processes on the surface [4]. The limited interlayer diffusion on Cu and Ag (001) surfaces strongly influences the pattern formation [14,34]. Ripples are only observed for grazing incidence ion sputtering [34,35]. The fast and in-situ characterization of such structured surfaces is an increasingly important task to understand the underlying mechanisms in pattern formation. Optical methods like light scattering have been used to characterize the statistically averaged properties of (periodically) rough surfaces [57,59,60]. The specular reflected beam also contains this information on the surface. Scatterometry uses this to characterize periodic structures from the polarization state of the reflected beam [66]. Such measurements are analysed by the computationally demanding Rigorous Coupled Wave Analysis approach. Alternatively, the Rayleigh Rice Theory (RRT) can be used for the analysis if the amplitude of the periodic structures is much smaller than the wavelength of the light. This requirement stems from the fact that RRT is a perturbation approach to the solution of Maxwell's equation at a sharp interface. We showed the applicability of RRT for the characterization of ion beam induced periodic etch features on a Ag(001) surface [33]. The surface plasmon resonance induced by such periodic patterns allow a sensitive, in-situ detection of the pattern characteristics with a technique like Reflection Anisotropy Spectroscopy (RAS).

The relation between a surface plasmon resonance and surface roughness was explored by Kretschmann and Kröger [61]. Their formulation of this optical response was generalized to oblique incidence reflection by Beaglehole [67]. Recently, Franta and Ohlidahl [52] reformulated and further generalized this reflection problem. The latter approach was successfully employed to analyze the recorded anisotropic plasmon resonance during ion sputtering of a Ag(001) surface [33]. The analysis of the recorded optical spectra shows a change in periodicity of the nanopattern with ion fluence. The average length scale of the nanopattern is found to be above 200nm. This allowed the straightforward determination of the periodicity. In this paper we will present the small roughness length scale limit of the RRT approach for anisotropy measurements. In this regime, the recorded spectra are well represented by a skewed Lorentzian line shape. This enables to characterize the pattern formation with three variables, its amplitude, position and width. The width of this line shape is directly related to the actual dielectric function at the surface and shows a broadening as a result of a finite size effect. Although the energy position reflects the length scale, its relation is complex. The amplitude will be shown to be related to both roughness amplitude and its length scale.

## 6.2 Experimental results

The ion beam erosion experiments were performed on a single crystalline Ag(001) sample in a UHV system [33]. A RAS instrument is used to measure the normalized difference in reflectivity $r$ of two orthogonal directions on the surface:

$$\frac{\Delta r}{r} = 2\frac{r_{\perp} - r_{\|}}{r_{\perp} + r_{\|}} \tag{6.1}$$

A home built RAS instrument based on a Photo Elastic Modulator (PEM) is used [19, 62]. A lock-in is tuned to the second harmonic of the PEM frequency to measure the real part of eq. 6.1. The parallel direction is chosen with respect to the incident ion beam.

Figure 6.1 shows the optical reflection anisotropy spectra during bombardment of a Ag(001) surface with 2keV Ar ions at a polar angle of incidence of 80° with the normal along the $< 110 >$ azimuth. An ion current of $5\mu A/cm^2$ measured at normal incidence was used while the substrate was at a temperature of 320K. Grazing incidence sputtering results in a plasmon resonance that grows with sputter time and displays a small red shift of its resonance energy. The value of the resonance energy indicates that the characteristic periodicity of the nanoripples is considerably smaller than the wavelength of the light used [24].

## 6.3 Optical characterisation of nanostructured surfaces

The change in reflection as a result of a rough interface can be described by the Rayleigh Rice approach. Using the notation of Franta and Ohlidahl [52], this perturbation can be written for a normal incident light beam as:

$$\hat{r}_{\perp,\|} = \hat{r}^{(0)}_{\perp,\|} + \sigma^2 \int_{-\infty}^{\infty}\int_{-\infty}^{\infty} \hat{f}_{\perp,\|}(\vec{K}, k_0) \times w(\vec{K}) d\vec{K} \tag{6.2}$$

where $\hat{r}^{(0)}_{\perp,\|}$ is the reflectivity of the unperturbed surface, $\sigma$ the rms value of the surface height and $w$ the normalized Power Spectral Density Function

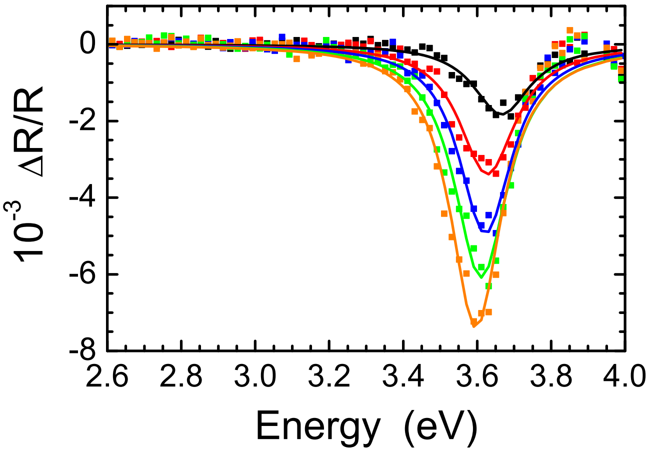

Figure 6.1: (symbols) RAS spectra obtained during Ar$^+$ ion sputtering at a polar angle of 80° with the normal. The spectra displayed were obtained during a total sputtering time of 960 min. and are at an interval of 180 min. The solid line represent the fit of a skewed Lorentzian as discussed in the text.

(PSDF), spanned by the spatial wave vector $\vec{K}$ of the surface. The light interaction is determined by the kernel $f_{\perp,\parallel}$, which depends on the wave vector of the incident light $k_0$ and $\vec{K}$. With the normalized parameters

$$\hat{b} = \sqrt{\left(\frac{k_0}{K}\right)^2 - 1} \tag{6.3}$$

$$\hat{c} = \sqrt{\left(\frac{k_0}{K}\right)^2 \cdot \epsilon - 1} \tag{6.4}$$

$$K = \sqrt{K_\perp^2 + K_\parallel^2} \tag{6.5}$$

the kernel $f_\perp$ for normal incidence reflection can be written as:

$$\hat{f}_\perp(K_\parallel) = -2k_0 r^{(0)}|K| \left( \frac{k_0}{|K|}\sqrt{\epsilon} + \frac{(\hat{b}-\hat{c})\left(\left(\frac{K_\parallel}{K}\right)^2 + \hat{b}\hat{c}\right)}{1+\hat{b}\hat{c}} \right) \tag{6.6}$$

For $\hat{f}_\parallel$ an analogous expression is found.

In the displayed RAS measurement an anisotropically rough surface on an optically isotropic substrate is probed. The RAS spectra can be related to the RRT by:

$$\frac{\Delta r}{r} = \frac{\sigma^2}{\hat{r}^{(0)}} \int_{-\infty}^{\infty} \int_{-\infty}^{\infty} (\hat{f_\perp} - \hat{f_\|}) w(\vec{K}) d\vec{K} \tag{6.7}$$

Only the difference in the kernel $\hat{f}$ for the two orthogonal directions is required, eliminating all isotropic contributions:

$$\hat{f_\perp} - \hat{f_\|} = -2k_0 \hat{r}^{(0)} |K| \frac{(\hat{b} - \hat{c})}{(1 + \hat{b}\hat{c})} \cdot \cos 2\phi \tag{6.8}$$

The angle $\phi$ represents the direction of $\vec{K}$ with respect to the parallel direction. The $cos2\phi$ term selects the anisotropic part of $w(\vec{K})$. Roughness contributions parallel to the ion beam are represented by a negative signal in the RAS spectra, while the perpendicular contribution provides a positive response.

Figure 6.2 shows the influence of the average periodicity on RAS spectra for a Gaussian roughness distribution. For an average spatial wave vector of $10\mu m^{-1}$ and below, the RAS spectra show a considerable change in resonance energy, width and intensity. Note the slight feature at 3.3 eV, which is not observed in the experimental data, see fig. 6.1. This is due to the use of the Palik data [68] of Ag in this calculation. At this energy, two data sets were merged in this table leading to a slight discontinuity. A spatial wave vector above $10\mu m^{-1}$ changes the intensity of the resonance, while its resonance energy shows a negligible shift. The small sensitivity of the resonance energy towards the periodicity in this range is well known and is directly obtained in the RRT approach for $K >> k_0$. This fact allows to simplify the anisotropy of the kernel in this range:

$$\hat{f_\perp} - \hat{f_\|} = -2ik_0 \hat{r}^{(0)} |\vec{K}| \frac{\epsilon - 1}{\epsilon + 1} \cos 2\phi \tag{6.9}$$

The kernel is reduced to a modulation of the plasmon optical resonance function $\frac{\epsilon-1}{\epsilon+1}$. Both rms roughness and spatial periodicity contribute in a similar way to the strength of this kernel. The anisotropic optical response is found by integrating the product of the kernel and the specific PSDF:

$$\frac{\Delta r}{r} = -2ik_0 \sigma^2 \frac{\epsilon - 1}{\epsilon + 1} \int_{-\infty}^{\infty} \int_{-\infty}^{\infty} |\vec{K}| \cos 2\phi w(\vec{K}) d\vec{(}K) \tag{6.10}$$

For a 1D ripple pattern with a Gaussian distribution centered around a spatial wavevector $K_0$ this integration leads to:

$$\frac{\Delta r}{r} = -2ik_0 \sigma^2 K_0 \frac{\epsilon - 1}{\epsilon + 1} \tag{6.11}$$

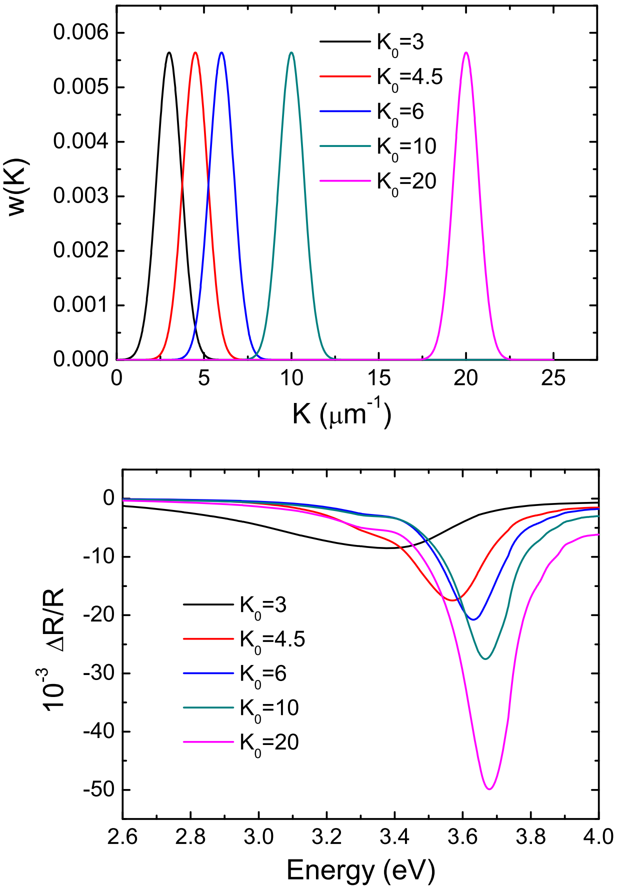

Figure 6.2: a) A Gaussian spectral density distributions with different average spatial wave vector $\vec{K}_0$. b) Calculated RAS spectra for the various spectral density distributions displayed in a).

Note that this result does not depend on the actual width of the distribution. Only the product of the rms roughness and the average spatial wavevector $K_0$ determines the amplitude. This indicates that one can not distinguish between the two in the small roughness region. This simplification is only obtained for the anisotropic reflection of an anisotropic pattern. On an isotropic randomly rough surface the isotropic contributions to the kernel show additional features [61].

The dielectric function of silver around the resonance energy for several literature datasets [68–70] is displayed in fig.6.3. In the limited energy

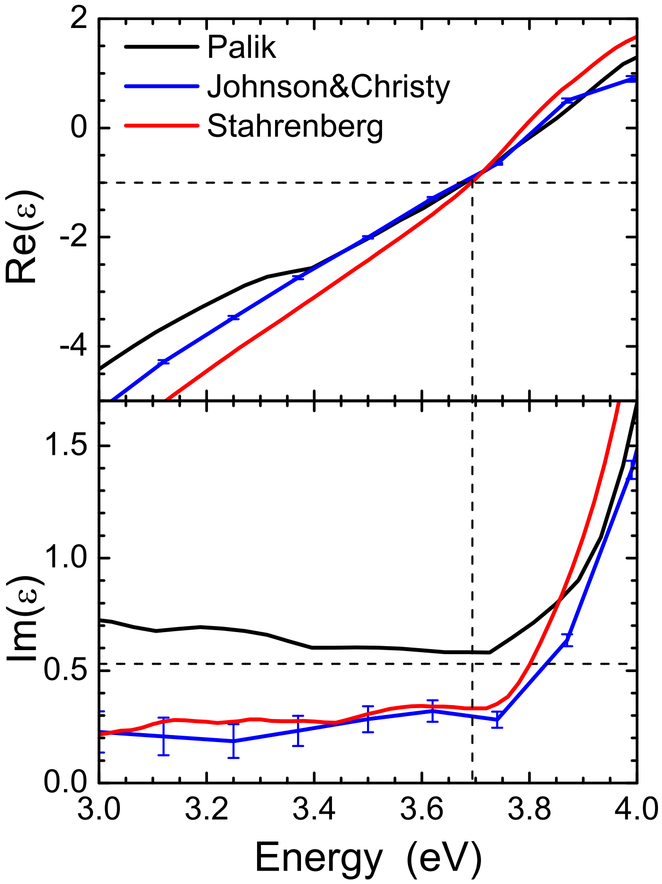

Figure 6.3: Dielectric function of Ag as reported by Palik [68], Johnson and Christy [69] and Stahrenberg et al. [70]

range of the observed resonance energy, the dielectric function can be approximated by: $\epsilon = -1 + \alpha(E - E_0) + i\gamma$ with $E_0$ the energy for which $Re(\epsilon) = -1$. The value of $\alpha = 6eV^{-1}$ is very similar for the three data sets, while the value of $\gamma$ is considerably larger for the Palik data set. The use of this dielectric function in eq. 6.11 gives for the real part of the optical anisotropy:

$$\frac{\Delta R}{R} = -4\sigma^2 K_0 k_0 \frac{\gamma/\alpha^2}{\Delta E^2 + (\gamma/\alpha)^2} \tag{6.12}$$

In this, $\Delta E$ is the energy difference with respect to the resonance position, $E - E_0$. For small scale roughness, the measured plasmon resonance is only sensitive for the product of the average reciprocal roughness periodicity, $K_0$

and the roughness variance $\sigma^2$. Note that $k_0$ is depending on E as well, which makes eq. 6.12 a skewed Lorentzian. A smaller roughness length scale enhances the optical response. Note that the use of a Drude form for the dielectric function would give a similar result, albeit that 3 parameters are required to characterize the Drude line shape. This results in a strong coupling between two of the parameters avoided by the approximation used above.

The skewed Lorentzian was fitted to the measured data and was found to represent the data set very well as displayed in fig. 6.1. Also the resonance energy $E_0$ was used as a fit parameter to accommodate for the observed slight red shift. This red shift from the energy position of 3.68eV (see fig. 6.3) indicates that the approximation $K >> k_0$ is no longer valid. However, the goodness of the fit shows that the skewed Lorentzian line shape can still be used and provides a good method to establish the resonance energy, the strength and the width of the line shape. These provide a valid experimental parameter set and they will be interpreted along the lines of eq. 6.12

## 6.4 Time evolution of the induced roughness

The change in the RAS spectra with sputter time is quantified by the fit parameters displayed in fig. 6.4. The width of the resonance feature is about constant, providing $\gamma = 0.53$. This value is quite similar to that found in the Palik data, but considerably higher than the more accurate values reported by Johnson and Christy [69] and Stahrenberg [70], see fig. 6.3. We attribute this to a reduced electron mean free path on the silver surface as a result of the induced roughness. To verify this, we also measured the RAS signal after sputtering at 250K. This gives a similar pattern with a smaller characteristic length scale [34]. The RAS spectrum shows a resonance energy at 3.68 eV, i.e at $Re(\epsilon) = -1$ and a peak width with $\gamma = 0.65$. This width is 20% higher than at 320K, attributed to a further reduced electron mean free path as a result of the smaller roughness length scale at the low temperature.

The development of the resonance energy with time directly reflects the increase of the average roughness length scale. The fit with a skewed Lorentzian allows to establish the resonance energy with great accuracy. It is tempting to translate the resonance energy shift into a length scale. However, we found in simulations a strong correlation between the average spatial wave vector and the width of the distribution with respect to the resonance energy. As a consequence, without knowledge of the distribution width, the resonance energy can not be used to extract the periodicity as was possible for less grazing incidence ion sputtering [33]. The goodness of fit should not hide the fact that eq.6.12 is used outside its derivation limits.

The increase of the strength of the resonance is reflected by the parameter $\sigma^2 K_0$. Because the ripple periodicity increases with sputter time, the observed change is the result of an increase in the roughness variance. An estimate of the surface roughness can be obtained by assuming a reasonable ripple periodicity. For a periodicity of 100 nm a roughness of $\sigma = 0.4$nm is evaluated for the highest ion dose. This value is very reasonable in view of previous results [34]. The observed linear increase of $\sigma^2 K_0$ with sputter time indicates that $\sigma \propto t^\beta$ with $\beta > 0.5$. A much higher value of this critical exponent is not likely.

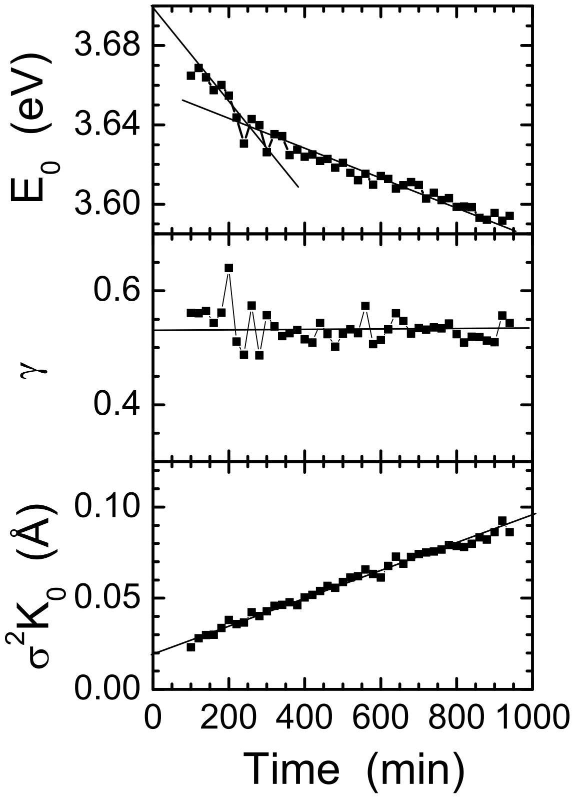

Figure 6.4: Result of the fit of the skewed Lorentzian on the measured RAS spectra. Shown are the time development of the resonance energy $E_0$, the width $\gamma$ and the amplitude $\sigma^2 K_0$. The lines are a guide to the eye.

## 6.5 Conclusion

Grazing incidence ion sputtering of a Ag(001) surface results in a ripple structure whose time development was measured with RAS. A slight red shift of the plasmon resonance energy with time is observed in the optical spectra. The average periodicity of these ripples is around 200 nm, i.e. at the lower border for the observation of a resonance shift as a result of surface roughness. A small length scale limit of the RRT approach was derived that shows that in this limit the influence of roughness and periodicity can no longer be distinguished. An appropriate approximation of the silver dielectric function shows that the measured spectra are well represented with a skewed Lorentzian line shape. This line shape enables a quantitative analysis. The width of the measured plasmon resonance shows that the induced ripples alter the actual dielectric function of silver at the surface. This alteration is the result of the reduced electron mean free path as a result of the surface roughness.

# CHAPTER 7

# Optical anisotropy induced by grazing incidence homoepitaxial growth on Ag(001)

## 7.1 Grazing incidence deposition of Cu on Cu(001)

Grazing incidence deposition is nowadays a versatile way of preparing thin films and coating. Unlike normal incidence homoepitaxy, where the symmetry of the growing surface features is determined by the underlying substrate, grazing incidence deposition induces a strong anisotropy. Initially it was thought that this anisotropy was solely the result of the shadowing effect caused by surface features blocking some trajectories of incoming atoms. Experimental studies [29, 71–78] however, show that this anisotropic growth mode is not only caused by the shadowing effect, but initiated by an attractive force between surface and incoming atoms. This leads to a heterogeneity in the incident flux: local indentations receive relatively little flux, while more flux is directed to protrusions. This so-called steering effect does not only play a role in multilayer growth, but already influences sub-monolayer growth. The influence of steering is determined by the interaction potential between the incoming atom and the surface. Simulations with an accelerated kinetic Monte Carlo scheme and diffraction experiments were combined by Rabbering [79], to determine this potential.

The surface morphology calculations shown in this chapter were made by Rabbering [79] and are used to evaluate the optical anisotropy during grazing incidence growth and will be briefly discussed, as well as their comparison to previous experimental results. The morphology simulations encompass two ingredients. The first ingredient is the deposition event itself, which depends on the interaction potential and, most importantly, on the surface morphology. The interaction-potential was modeled by a modified Lennard-Jones potential (eq. 7.1), as described by Rabbering et al. [80]. Its strength was found by comparison with experimental data.

$$\phi(r) = \frac{C_{10}}{(r/\xi)^{10}} - \frac{C_8}{(r/\xi)^8} - \frac{C_6}{(r/\xi)^6} \tag{7.1}$$

with $C_{10} = 1.843$eV, $C_8 = 2.118$eV and $C_6 = 0.1689$eV, nearest neighbour distance $\xi = 2.55$Å and $r$ the distance between the surface and the incoming atom.

The second ingredient of the simulation is the diffusion on the surface. The deposition rate for the simulations is typically 2.5 ML/min. Figure 7.1a shows all possible diffusion paths for an adatom on a flat surface, if one assumes no overhangs. On the positions 1-7 there can be either an atom present or a vacancy, resulting in 128 possible movements. Because of symmetry reasons, there are 72 unique paths, which all have a specific activation barrier. The values of these intralayer barriers were obtained from

EAM Embedded Atom Method (EAM) by Biham et al. [81]. Biham et al. verified this dataset by comparing submonolayer growth simulations with experimentally available data.

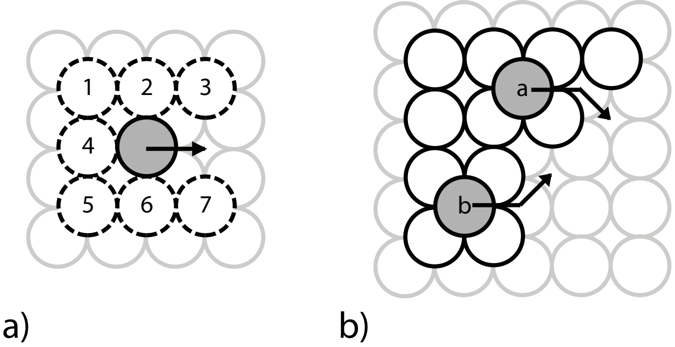

Figure 7.1: Possible movements of an adatom on a fcc(001) surface. a) The possible intralayer diffusion paths. On positions 1-7 there can be an atom present. b) The two interlayer diffusion path, either of the kink site (a) or over the closed-step edge (b)

The experimental work of Ehrlich [82] and the theoretical work of Schwoebel [83] showed that additional barriers exist for diffusion over step edges. These two additional interlayer barriers for a fcc(001) surface (see figure 7.1b) are very important in multilayer growth. These barriers were determined by a combination of simulations and helium diffraction experiments [37]. The resulting morphologies after multilayer growth were compared to experimental data from both STM (Stoian [84]) and HR-LEED (Rabbering [79]) and were found to be in good agreement [78]. As an illustration, figure 7.2 shows characteristic simulated morphologies and STM images obtained in homoepitaxy experiments for the growth of 40ML of Cu on Cu(001) at grazing incidence (80°) and at a temperature of 270, 250 and 220/230K.

At 270K an elongation of the adatom structures parallel to the plane of incidence is observed, while at 250K mounds with the elongation both parallel and perpendicular are observed. The simulations at 230K predict mounds elongated parallel to the plane of incidence, which are also observed in HR-LEED, but experimentally difficult to measure in STM. The experimental snapshots show that the simulation can be used to study the growth mode. Initially, grazing incidence growth results in the formation of mounds oriented perpendicular to the plane of incidence of the arriving atoms. A transition towards parallel orientation occurs at a coverage, that depends on temperature, incidence angle and growth rate, as shown by Shim et al [85].

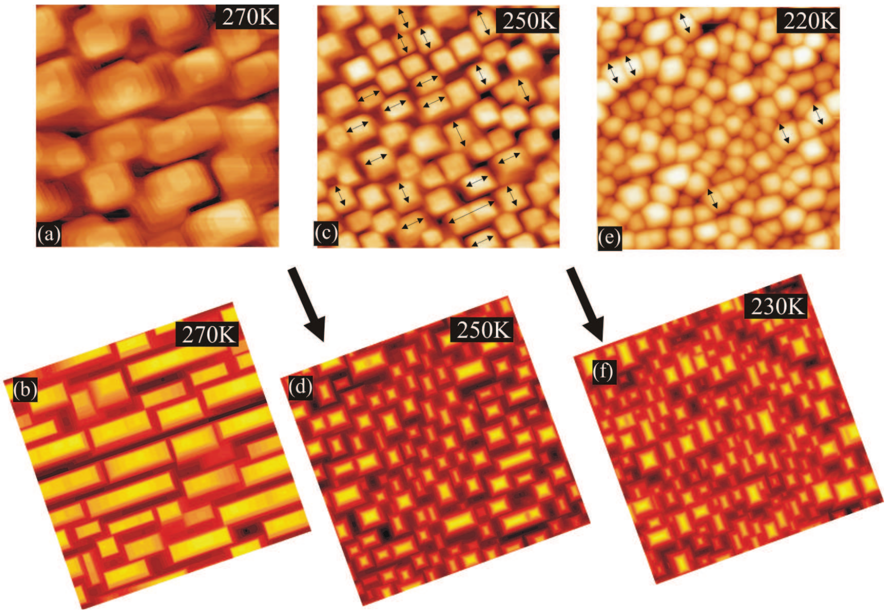

Figure 7.2: Comparison of the surface morphology after 40ML growth of Cu on Cu(001) at a polar angle of incidence of 80° and a temperature of 270K, 250K and 220/230K respectively. The top row shows experimentally obtained images [84] and the bottom row simulations [79]. The STM images have an image size of 145x145 nm and the simulated images are 130x130 nm. Black arrows indicate the plane of incidence.

The situation at 250K indicates that 40ML is the transition coverage under these conditions. The growth mode of Ag/Ag(001) is expected to be very similar to that of Cu/Cu(001). Therefore, the simulations described above will be used to calculate the optical response during grazing incidence homoepitaxial growth on Ag(001).

## 7.2 Simulated optical response

Although grazing incidence deposition leads to a rough surface on a large scale, it can be treated as a small deviation from a smooth surface. The optical response can thus be calculated by the Rayleigh-Rice theory (RRT) (see chapter 5). The power spectral density functions (PSDF) of the simulated morphologies were calculated by a Fast Fourier Transform (FFT) and used as the input for the RRT, to calculate the optical reflection difference spectra. The simulated surface area was in all cases 512x512 atoms. For a nearest neighbour distance of 2.87 Å for silver, this means that the field of view is about 145nm. As mentioned above, we use the kMC simulations results of copper for comparison with the silver experiments. To accommodate the difference between Cu and Ag, the temperatures are scaled by the melting temperature of Cu and Ag. In this temperature regime this leads to an about 25K lower temperature for Ag. All temperatures mentioned with reference to the simulated results are the original Cu(001) temperatures.

The surface morphologies in figure 7.3 were calculated for deposition at an angle of incidence of 85°, a sample temperature of 250K and a deposition rate of 2.5ML/min. Note that in the morphology images, the orientation of the anisotropic features is rotated by 90° at about 20ML. As shown in chapter 6, reflectance anisotropy spectroscopy, (RAS) is very sensitive for small scale roughness and could be used to monitor this change in orientation during deposition.

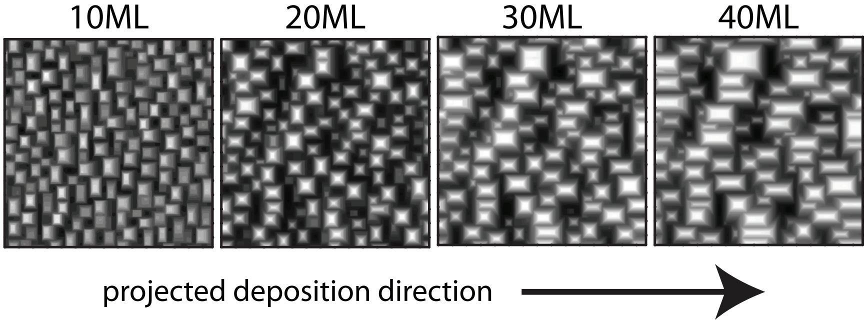

Figure 7.3: Surface morphologies from simulation at different coverages. The angle of incidence of the deposition source is 85° and the sample temperature is 250K. The projected deposition direction is indicated with the arrow. The size of the images is 145x145nm.

Figure 7.4 shows the calculated RAS spectra for the simulated growth at a sample temperature of 250K for three different angles of incidence. There is a single optical feature, revealing the shape anisotropy of the surface morphologies. In all simulations, the feature size is below 50nm. As shown in chapter 6, for one-dimensional small scale roughness the reflectance difference can be approximated by eq 7.2. For this single resonance, shape and position of the peak is determined by $k_0 \cdot (\epsilon - 1)/(\epsilon + 1)$, but the strength of the peak depends on the product of roughness and average periodicity $\sigma^2 \cdot \vec{K}_0$.

$$\frac{\Delta r}{r} = -2ik_0\sigma^2\vec{K}_0 \cdot \frac{(\epsilon - 1)}{(\epsilon + 1)} \tag{7.2}$$

where $\epsilon$ is the dielectric function of silver, $\Delta r/r$ the normalized difference in reflectivity, $k_0$ the wavevector of the incoming light, $\sigma$ the roughness of the surface and $\vec{K}_0$ the mean reciprocal length of the surface features.

The morphologies in figure 7.3 have periodicities in two directions, i.e. parallel and perpendicular to the plane of incidence, with average periodicities $K_{0,\|}$ and $K_{0,\perp}$ and heights $\sigma_\|$ and $\sigma_\perp$. The reflectance difference for these morphologies will be a superposition of the resonances for both directions and is given by eq 7.3. In the initial stage the mounds are elongated perpendicular to the incoming beam and thus $\sigma_\|^2 K_{0,\|} < \sigma_\perp^2 K_{0,\perp}$, resulting in a negative peak at the plasmon energy. On the contrary, for higher coverages $\sigma_\|^2 K_{0,\|} > \sigma_\perp^2 K_{0,\perp}$ and the peak will become positive.

$$\frac{\Delta r}{r} = -2ik_0 \cdot \frac{(\epsilon - 1)}{(\epsilon + 1)} \cdot \left(\sigma_\|^2 K_{0,\|} - \sigma_\perp^2 K_{0,\perp}\right) \tag{7.3}$$

Two length scales can be identified on the simulated morphologies, namely the ordering of the mounds and the size of the mounds. Calculations show that the optical anisotropy is the result of mound shape anisotropy and barely depends on the difference in ordering of the mounds in both directions. The mound size is the smaller scale roughness and thus RAS is more sensitive for the mound shape anisotropy than to the ordering anisotropy. All information about the mound shape anisotropy of the surface features is solely located in the peak at 3.70eV.

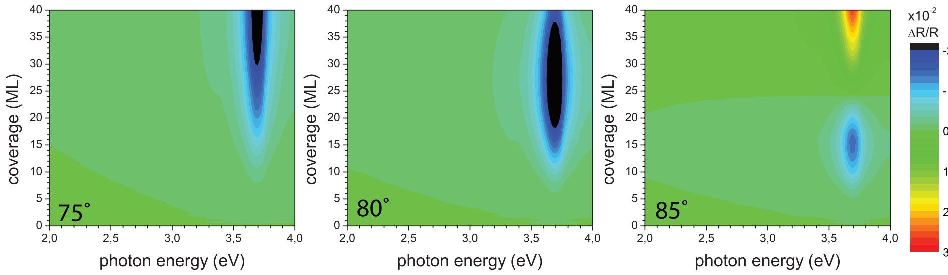

Figure 7.4: RAS spectra as calculated from the simulated morphologies at 250K, with different angles of incidence 75°, 80° and 85° and a deposition rate of 2.5 ML/min. The same color scale is used in all graphs.

In figure 7.5 the strength of the optical signal at the surface plasmon energy (3.70eV) is plotted as function of the coverage for three different angles of incidence. For an angle of incidence of 75°, the strength of the plasmon resonance is monotonously increasing, until it more or less saturates at 40 monolayers. For a more grazing angle of incidence of 80°, the anisotropy of the surface feature is stronger and the plasmon resonance initially increases more quickly. At about 28 monolayers, the strength starts to decrease, but the sign of the signal stays negative within the simulation window. For the most grazing angle of incidence of 85° the maximum of the signal strength is achieved already at about 14 monolayers. Again the signal decreases as function of coverage and at about 24 monolayers there is a transition of the anisotropy from perpendicular to parallel to the plane of deposition.

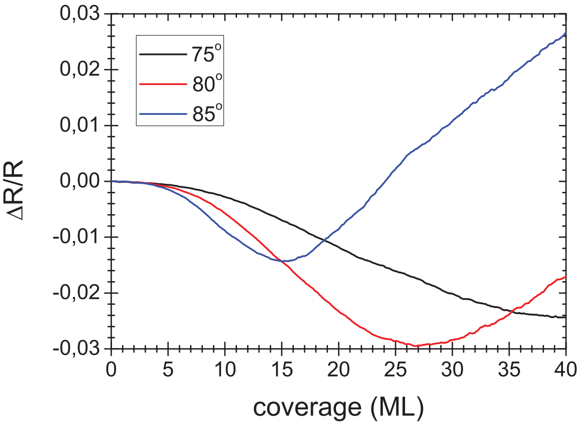

Figure 7.5: Reflectance difference at 3.70eV as function of coverage for an sample temperature of 250, different angles of incidence of 75°, 80° and 85° and a deposition rate of 2.5 ML/min.

It is highly probable that even with a deposition angle of 80° and 75° such a transition from perpendicular to parallel elongation occurs, but at a much higher coverage outside the simulation window. The larger the deposition angle, the sooner the transition occurs [85]. Experimentally, however an increasing angle implies a decreasing deposition rate. For comparison with experiments an angle of 80° is the best trade-off between deposition rate and anisotropy transition.

Figure 7.6 shows the calculated spectra for simulations at different sample temperatures at an angle of incidence of 80°. In figure 7.7 the corresponding optical anisotropy at the plasmon energy 3.70eV is plotted as function of coverage. It is clear that for the lower sample temperature the transition of the anisotropy occurs at a lower coverage, but the strength of the signal is slightly smaller as well. This implies that the amount of anisotropy is

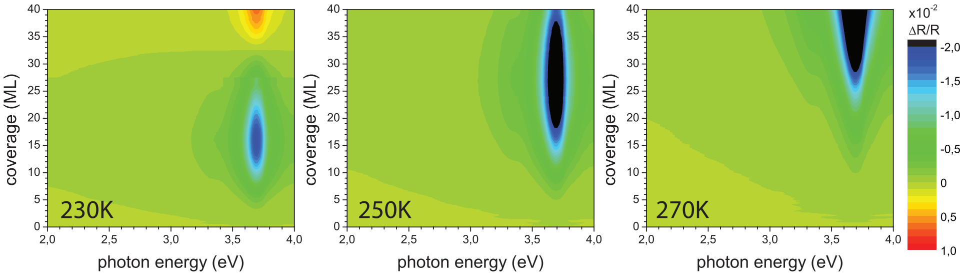

Figure 7.6: RAS spectra as calculated from the simulated morphologies with an angle of incidence of 80°, for different sample temperatures of 230K, 250K and 270K and a deposition rate of 2.5 ML/min. Note that the same color scale is used for the three different temperatures, but this scale differs from figure 7.4.

smaller for lower temperatures, assuming the height of the modulation is the same in both directions.

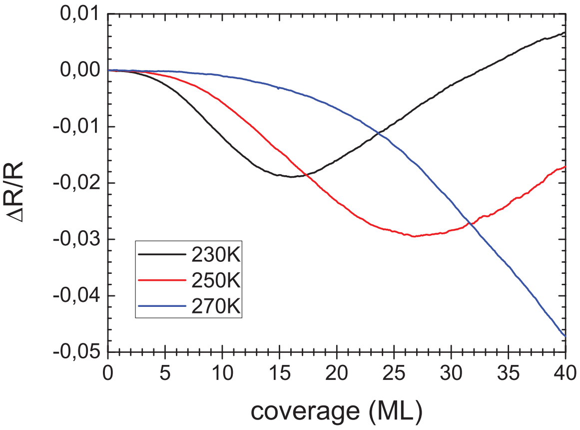

Figure 7.7: Reflectance difference at 3.70eV as function of coverage for an angle of incidence of 80°, sample temperatures of 230K, 250K and 270K and a deposition rate of 2.5.

## 7.3 Measurements

The experimental data was obtained during homoepitaxy experiments, performed on a single crystalline Ag(001) sample in an UHV system. The sample was cleaned with multiple ion bombardment and anneal cycles. For the RAS measurements, a home built system was used, as described in chapter 4. A first (preliminary) result is shown in figure 7.8. The optical data is obtained with RAS while depositing Ag on Ag(001), at an angle of incidence of 80° and a sample temperature of 250K. This sample temperature of 250K corresponds roughly with the simulated data at 270K. Note that in the initial stage some optical data is missing, indicated by the grey area. Since only an optical response was expected around the surface plasmon energy, initially a smaller photon energy range was used, providing enhanced time resolution.

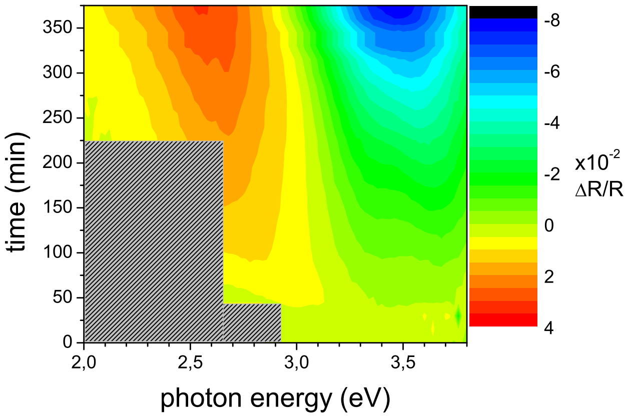

Figure 7.8: Reflectance difference measured as function of time during deposition of Ag on Ag(001) with an angle of incidence of 80° and a sample temperature of 250K. Deposition rate is estimated at 12 ML/hr. Optical data is not recorded for the grey areas.

At the surface plasmon energy, a negative peaks evolves, as predicted in the calculations. No saturation of the peak strength or change in sign is visible within this experiment. The deposition rate had to be calibrated in a different geometry, but was roughly estimated at 1 monolayer in 5 minutes. Therefore, the final coverage is estimated at about 72 monolayers.

Surprisingly, at lower photon energies there is also a peak with opposite sign evolving with increasing coverage. Also for this peak no change in sign is observed within this experimental window. This peak could indicate a much larger periodicity in the direction perpendicular to the elongation, very alike the results in chapter 4.

A second experiment was done at the same angle of incidence, but with a lower sample temperature of 200K. The deposition rate is calibrated at the same rate, so the final coverage is roughly 280ML. There is a negative

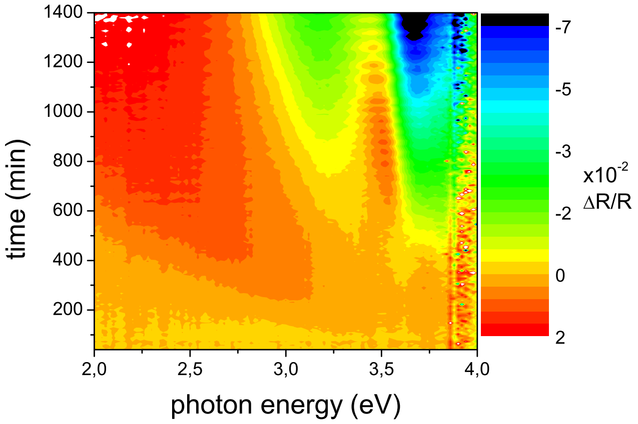

Figure 7.9: Reflectance difference measured as function of time during deposition of Ag on Ag(001) with an angle of incidence of 80° and a sample temperature of 200K. Deposition rate is estimated at 12 ML/hr.

peak evolving at the plasmon energy, but again no change of sign is observed. Besides this peak at the plasmon energy, there are multiple additional peaks visible at different lower energies. The spectrum is a superposition of all resonance peaks and since the number of peaks is not known, it is impossible to distinguish the exact position and shape of each of these peaks. Note that the time dependent oscillations in the optical signal (most pronounced around 3.5eV and longer deposition times) are the result of an instability in the optics, caused by fluctuations of the room temperature.

## 7.4 Conclusion

Although predicted with simulations, no change in sign of the optical anisotropy, indicating the rotation of the anisotropy during deposition, was observed. However, the strength of the optical response was of the same order of magnitude as in the simulations ($\sim 10^{-2}$). This indicates that the roughness and periodicity in the simulations are comparable to the observed resonance features. One of the biggest problems with these preliminary results, is the calibration of the deposition source. The exact deposition rate is not known and is strongly influenced by the geometry of the experiment. Furthermore, it might also strongly vary with time. For an angle of incidence of 80°, a source-sample distance of about 12 cm and a beam diameter of 6mm, the deposition rate differs ±3.4% within the 4mm of the spot of the optical probe, due to variation in distance and deposition angle. These variations can have some influence on the growth mode and it is therefore not completely certain that the transition should have been occurred within the experimental time window. Also the reproducibility of the results has still to be proven. More optical experiments are needed to rule out influences of sample preparation, deposition rate and optics instability by variations in room temperature.

In both experiments presented in this chapter, a complex superposition of resonance peaks was measured. Most of these peaks appear energies below the plasmon energy and can be associated with length scales larger than approximately 150nm. Since the window size in both simulated and experimental morphological data is too small for these length scales, it is not possible to compare the experimental data with calculated spectra. Therefore a proper model for the PSDF of these surfaces can not be made and a proper RRT calculation is not possible.

# Bibliography

[1] M. Raza, E. Kooij, A. v. Silfhout, and B. Poelsema, Langmuir **26 (15)**, 12962 (2010).

[2] M. Navez, C. Sella, and D. Chaperot, C.R. Acad. Sci. Paris **254**, 240 (1962).

[3] G. Carter, B. Navinsek, and J. Whitton, *Sputtering by Particle Bombardment II*, Springer-Verlag, 1983.

[4] R. M. Bradley and J. M. E. Harper, J. Vac. Sci. Technol. A **6**, 2390 (1988).

[5] W. W. Mullins, J. Appl. Phys. **30**, 77 (1959).

[6] R. Cuerno and A.-L. Barabási, Phys. Rev. Lett. **74**, 4746 (1995).

[7] P. Broekmann, A. Mewe, H. Wormeester, and B. Poelsema, Phys. Rev. Lett. **89**, 146102 (2002).

[8] U. Valbusa, C. Boragno, and F. Buatier de Mongeot, J. Phys.: Condens. Matter **14**, 8153 (2002).

[9] C. G. Kalff M and M. T. . S. S. . 103, Surf. Sci. **486**, 103 (2001).

[10] M. Murty et al., Phys. Rev. Lett. **80**, 4713 (1998).

[11] J. Naumann, J. Osing, A. Quinn, and I. Shvets, Surf. Sci. **388**, 212 (1997).

[12] S. Rusponi, C. Boragno, and U. Valbusa, Phys. Rev. Lett. **74**, 2795 (1997).

[13] S. Rusponi, G. Costantini, C. Boragno, and U. Valbusa, Phys. Rev. Lett. **81**, 4184 (1998).

[14] W. L. Chan and E. Chason, J. Appl. Phys. **101**, 121301 (2007).

[15] J. Drotar, Y. Zhao, T. Lu, and G.-C. Wang, Phys. Rev. E **59**, 117 (1999).

[16] C. Boragno et al., Phys. Rev. B **65** (2002).

[17] P. Weightman, D. S. Martin, R. J. Cole, and T. Farrell, Rep. Prog. Phys. **68**, 1251 (2005).

[18] D. Aspnes and A. Studna, Phys. Rev. Lett. **54**, 1957 (1985).

[19] D. E. Aspnes, J. P. Harbison, A. A. Studna, and L. T. Florez, J. Va. Sc. Technol. A **6**, 1327 (1988).

[20] L. D. Sun, M. Hohage, P. Zeppenfeld, R. Balderas-Navarro, and K. Hingerl, Phys. Rev. Lett. **96**, 016105 (2006).

[21] L. Sun, M. Hohage, P. Zeppenfeld, C. Deisl, and E. Bertel, Surf. Sci. **600**, L281L285 (2006).

[22] L. Sun, M. Hohage, P. Zeppenfeld, R. Balderas-Navarro, and H. K., Phys. Rev. Lett. **90**, 106104 (2003).

[23] R. Ehlert et al., J.Opt.Soc.Am.B **27**, 981 (2010).

[24] H. Raether, *Surface plasmons on smooth and rough surfaces and on gratings*, volume 111 of *Springer Tracts in Modern Physics*, Springer, Berlin, 1988.

[25] W. Chan, N. Pavenayotin, and E. Chason, Phys. Rev. B **69**, 245413 (2004).

[26] Z. Sobiesierski, D. I. Westwood, and C. C. Matthai, Journal of Physics: Condensed Matter **10**, 1 (1998).

[27] M. Garfinkel, J. Tiemann, and W. Engeler, Phys. Rev. **148**, 695 (1966).

[28] H. Hansen et al., Phys. Rev. B **73**, 235414 (2006).

[29] L. C. Jorritsma, M. Bijnagte, G. Rosenfeld, and B. Poelsema, Phys. Rev. Lett. **78**, 911 (1997).

[30] C. Teichert, C. Ammer, and M. Klaua, Phys. Stat. Sol. A **146**, 223 (1994).

[31] J. Erlebacher, M. Aziz, E. Chason, M. Sinclair, and J. Floro, Phys. Rev. Lett. **82**, 2330 (1999).

[32] S. Habenicht, W. Bolse, K. P. Lieb, K. Reimann, and U. Geyer, Phys. Rev. B **60**, R2200 (1999).

[33] F. Everts, H. Wormeester, and B. Poelsema, Phys. Rev. B **78**, 155419 (2008).

[34] H. Wormeester and B. Poelsema, Journal of Physics Condensed Matter **21**, 224002 (2009).

[35] S. van Dijken, D. de Bruin, and B. Poelsema, Phys. Rev. Lett. **86**, 4608 (2001).

[36] R. Gerlach, T. Maroutian, L. Douillard, D. Martinotti, and H.-J. Ernst, Surf. Sci. **480**, 97 (2001).

[37] F. L. W. Rabbering, H. Wormeester, F. Everts, and B. Poelsema, Phys. Rev. B **79**, 075402 (2009).

[38] R. Kunkel, B. Poelsema, L. K. Verheij, and G. Comsa, Phys. Rev. Lett. **65**, 733 (1990).

[39] S. Facsko et al., Science **285**, 1551 (1999).

[40] B. Ziberi, F. Frost, T. Höche, and B. Rauschenbach, Phys. Rev. B **72**, 235310 (2005).

[41] T. Aste and U. Valbusa, New Journal of Physics **7**, 122 (2005).

[42] M. M. Ovsyanko, *Ion sculpting of Cu(001)*, PhD thesis, Twente University, 2006.

[43] T. C. Kim et al., Phys. Rev. Lett. **92**, 246104 (2004).

[44] S. Habenicht, K. P. Lieb, J. Koch, and A. D. Wieck, Phys. Rev. B **65**, 115327 (2002).

[45] D. A. G. Bruggeman, Ann. Physik **24**, 636 (1935).

[46] D. Martin, R. Cole, and P. Weightman, Phys. Rev. B **72**, 035408 (2005).

[47] M. Rocca, F. Moresco, and U. Valbusa, Phys. Rev. B **45**, 1399 (1992).

[48] J. Wollschläger, E. Luo, and M. Henzler, Phys. Rev. B **57**, 15541 (1998).

[49] M. Horn-vonHoegen, Z. Kristallogr. **214**, 591 (1999).

[50] H. Niehus, W. Heiland, and E. Taglauer, Surf. Sci. Rep. **17**, 213 (1993).

[51] B. Poelsema, L. K. Verhey, and A. L. Boers, Surf. Sci. **55**, 445 (1976).

[52] D. Franta and I. Ohlídal, Opt. Commun. **248**, 459 (2005).

[53] J. W. Evans, P. A. Thiel, and M. C. Bartelt, Surf. Sci. Rep. **61**, 1 (2006).

[54] J. K. Zuo and J. F. Wendelken, Phys. Rev. Lett. **78**, 2791 (1997).

[55] J. Munoz-Garcia, M. Castro, and R. Cuerno, Phys. Rev. Lett. **96**, 086101 (2006).

[56] A. L. Barabási and H. E. Stanley, *Fractal concepts in surface growth*, Cambridge University Press, 1995.

[57] Y. Zhao, G.-C. Wang, and T.-M. Lu, *Characterization of amorphous and crystalline rough surface: principles and applications*, volume 37 of *Experimental methods in physical sciences*, Academic Press, 2001.

[58] M. Raible, S. J. Linz, and P. Hänggi, Phys. Rev. E **62**, 1691 (2000).

[59] J. Erlebacher, M. Aziz, E. Chason, M. Sinclair, and F. J.A., Phys. Rev. Lett. **84**, 5800 (2000).

[60] E. Chason, M. Sinclair, J. Floro, J. Hunter, and R. Hwang, Appl. Phys. Lett. **72**, 3276 (1998).

[61] E. Kretschmann and E. Kröger, J. Opt. Soc. Am. **65**, 150 (1975).

[62] J.-T. Zettler et al., J. of Crystal Growth **195**, 151 (1998).

[63] A. Politano and G. Chiarello, J. Phys. D: Appl. Phys. **43** (2010).

[64] H. Wormeester, F. Everts, and B. Poelsema, Thin Solid Films **to be published** (2010).

[65] F. Everts, H. Wormeester, and B. Poelsema, Phys. Rev. B **081415(R)** (2010).

[66] H.-T. Huang and F. L. Terry J, Thin Solid Films **455-456**, 828 (2004).

[67] D. Beaglehole, Physica B **100**, 163 (1980).

[68] E. D. Palik, *Handbook of optical constants of solids*, volume 1, Academic Press, 1997.

[69] P. B. Johnson and R. W. Christy, Phys. Rev. B **6**, 4370 (1972).

[70] K. Stahrenberg, T. Herrmann, K. Wilmers, N. Esser, and W. Richter, Phys. Rev. B **64**, 115111 (2001).

[71] H. Dürr, J. Wendelken, and J. K. Zuo, Surf. Sci. **328**, L527 (1995).

[72] L. C. Jorritsma, *Growth anisotropy in Cu(001) homoepitaxy.*, PhD thesis, University of Twente, 1997.

[73] S. van Dijken, L. Jorritsma, and B. Poelsema, Phys. Rev. Lett. **4038**, 1999 (82).

[74] S. van Dijken, G. Di Santo, and B. Poelsema, Appl. Phys. Lett. **77**, 2030 (2000).

[75] S. van Dijken, L. Jorritsma, and B. Poelsema, Phys. Rev. B **61**, 14047 (2000).

[76] S. van Dijken, G. Di Santo, and B. Poelsema, Phys. Rev. B **63**, 104431 (2001).

[77] H. Wormeester and B. Poelsema, Phys. Rev. B. **66**, 165406 (2002).

[78] F. L. W. Rabbering, G. Stoian, v. R. Gastel, H. Wormeester, and B. Poelsema, Phys. Rev. B **81**, 115425 (2010).

[79] F. L. W. Rabbering, *On the interplay of steering and interlayer diffusion in Cu(001) homoepitaxy*, PhD thesis, University of Twente, 2008.

[80] F. Rabbering et al., Phys. Rev. Lett. **103**, 096105 (2009).

[81] O. Biham et al., Surf. Sci. **400**, 29 (1998).

[82] G. Ehrlich and F. Hudda, J. Chem. Phys. **44**, 1039 (1966).

[83] R. Schwoebel, J. Appl. Phys. **40**, 619 (1969).

[84] G. Stoian, *Primary effects in ripple formation induced by erosion and growth of Cu(001)*, PhD thesis, University of Twente, 2008.

[85] Y. Shim and J. Amar, Phys. Rev. Lett. **98**, 046103 (2007).

# Summary

The creation of nanometre-scale patterns by self organization is of great interest, because of the possibility to cover large areas in a fast and cheap way. To be able to use this technique in an industrial environment, it is of great importance that we understand the underlying fundamental mechanisms. Often this is done by (ex-situ) analysis of the patterned surfaces after the self-organization process. However, to fully understand the pattern formation, an in-situ probe is needed. In this thesis we used an optical in-situ technique (Reflectance Anisotropy Spectroscopy) to measure the difference in reflection, due to the anisotropic patterning of surfaces. We developed a model to analyze the results and obtain the parameters that describe the main properties of the surface. In the various chapters we show the applicability of our model in different situations.

For pattern formation by ion erosion it is known that the experimental parameters, like substrate temperature, ion beam angle of incidence and ion energy, play a major role in the final morphology. However, the role of the azimuthal direction of the substrate is less well known. Often this parameter is considered of no substantial influence on the surface morphology, especially for isotropic surfaces. In chapter 3 we investigated this influence of the azimuthal direction on the pattern formation on Cu(001) for erosion with $\mathrm{Ar}^+$ ions by high resolution low energy electron diffraction (HR-LEED). Remarkably, even at small polar angles of incidence, there is a major difference for sputtering along the $\langle 110 \rangle$ and the $\langle 100 \rangle$ azimuthal directions, even for the 'isotropic' Cu(001) surface. For an angle of incidence of 10°, the fourfold symmetry is already broken for sputtering along the $\langle 100 \rangle$ direction, whereas for sputtering along the $\langle 110 \rangle$ direction this is not the case. Also, only for

sputtering along the ⟨100⟩ azimuthal direction Bradley-Harper behavior is observed, as the ripple orientation rotates 90° for increasing polar angles.

In chapter 4 the forming of ripple patterns on Ag(001) by ion erosion with a polar angle of incidence of 70° was in-situ studied by Reflectance Anisotropy Spectroscopy (RAS). The difference in reflection parallel to the ripples and perpendicular to the ripples was measured and analyzed with the Rayleigh-Rice theory (RRT). By assuming ripples with a distributed periodicity, the average periodicity and amplitude could be monitored as function of time for periodicities above 200nm. Since the measured optical spectra only showed a resonance in one direction, the assumption of a one dimensional ripple pattern was justified and resulted in an accurate description of the optical data. From this optical data, scaling exponents were determined to characterize the surface in the initial phase of pattern formation for various substrate temperatures. For an increasing substrate temperature larger length scales on the patterned surfaces were observed, although the time evolution behaves similar.

By changing the polar angle of incidence of the ion beam to 61.5°, the structures on the surface become two dimensional, i.e. the ripples become elongated pits. In chapter 5 we used RAS to monitor the development of these structures. In contrast to the optical spectra obtained on the ripple features, the measurements on the elongated pits show resonance peaks in both directions (e.g. positive and negative peaks in the spectra). This means that the one dimensional description, as used to describe the ripple features, is not sufficient in this situation. Therefore we used a two dimensional RRT model to describe the periodicities and roughnesses in both directions. Both a 2D Gaussian model, as well as the more physically realistic Edwards-Wilkinson model were used in the RRT model. The fit data with the Gaussian model resembles the measurements best and shows that the average periodicity between etch features is always larger parallel to the ion beam. Both directions grow in a similar way, but after saturation of the anisotropic roughness, the ordering along the beam direction starts to decrease.

By changing the polar angle of incidence of the ion beam to 80°, almost perfect ripple patterns evolve. The periodicity of these very shallow ripples is below 200nm and therefore the same analysis as used for the ripples patterns obtained at 70° angle of incidence, can not be used in this case. We showed that for these small periodicities, the strength of the resonance is depending on both the periodicity and roughness on the surface and therefore it is not possible to obtain these properties. However, the resonance can be described very well with a skewed Lorentzian line shape, which enables a quantitative analysis of the data. The width of this line shape is changing, indicating a change in this dielectric function by small scale roughness. This implies that the actual dielectric function of silver at the surface is slightly altered with respect to the bulk as a result of the reduced electron mean free path due to the small scale surface roughness.

In the final chapter 7, we studied the pattern formation by grazing incidence deposition as function of coverage. For grazing incidence deposition, the evolution of elongated surface features is expected. This surface anisotropy is enhanced due to an additional attractive force between the surface and the incoming atom ('steering'). Since the typical feature size is far below 200nm for both direction, only a nett resonance peak at the surface plasmon peak is expected due to this anistropic pattern. From simulations a change in direction of the anisotropy is expected at a certain coverage, which results in a change of sign of this resonance peak. However, in initial experiments we measured a complex superposition of resonance peaks, indicating ordering at different length scales. The change in sign however, was not measured. Therefore, more experiments are needed at different experimental conditions.

# Samenvatting

Het creëren van patronen op nanometer schaal door middel van zelf organisatie is interessant, vanwege de mogelijkheid om grote oppervlaktes op een goedkope en snelle manier te bedekken. Om deze techniek te kunnen gebruiken in een industriële omgeving, is het belangrijk dat we de onderliggende fundamentele mechanismen begrijpen. Dit wordt vaak gedaan door (ex-situ) analyse van de gestructureerde oppervlaktes na het zelf organisatie proces. Echter, om de patroon vorming helemaal te kunnen begrijpen is een in-situ waarneming nodig. In dit proefschrift gebruiken we een optische in-situ techniek (Reflectance Anistropy Spectroscopy) om het verschil in reflectie te meten, veroorzaakt door de anisotrope structurering van het oppervlak. We hebben een model ontwikkeld om de resultaten te analyseren en de parameters te verkrijgen die de belangrijkste eigenschappen van het oppervlak beschrijven. In de verschillende hoofdstukken laten we de toepasbaarheid zien van ons model voor verschillende situaties.

Voor de patroonvorming door middel van ionen erosie is het bekend dat experimentele parameters, zoals de temperatuur van het substraat, hoek van inval van de ionen bundel en de ionen energie, een belangrijke rol spelen in het tot stand komen van de uiteindelijke morfologie. Echter, de rol van de azimut van het substraat is minder bekend. Vaak wordt deze parameter beschouwd als onbelangrijk voor de oppervlakte morfologie, zeker voor isotrope oppervlakken. In hoofdstuk 3 hebben we met hoge resolutie elektronen diffractie (HR-LEED) gekeken naar de invloed van de azimut op de patroon vorming op Cu(001) voor erosie met $Ar^+$ ionen . Opmerkelijk genoeg is er zelfs voor kleine polaire hoeken van inval een groot verschil voor sputteren langs de $\langle 110 \rangle$ azimut en $\langle 100 \rangle$ azimut. Bij een hoek van inval van

10° is de viervoudige symmetrie al verbroken voor sputteren langs de $\langle 100\rangle$ azimut, terwijl voor sputteren langs de $\langle 110\rangle$ azimut dit nog niet het geval is. Ook is er alleen voor sputteren langs de $\langle 100\rangle$ azimut Bradley-Harper gedrag geobserveerd. De oriëntatie van de groeven draait over 90° voor grotere polaire hoeken van inval.

In hoofdstuk 4 is de vorming van groeven op Ag(001) door middel van ionen erosie met een polaire hoek van inval van 70° in-situ bestudeerd by RAS. Het verschil tussen de reflectie parallel met de groeven en loodrecht op de groeven was gemeten en geanalyseerd door middel van de Rayleigh-Rice Theory (RRT). Door aan te nemen dat er groeven ontstaan met een distributieve periodiciteit, konden de gemiddelde periodiciteit en hoogte gevolgd worden in tijd, voor een periodiciteit boven 200nm. Aangezien de gemeten optische spectra alleen een resonantie geven in één richting, is de aanname voor één dimensionale groeven gerechtvaardigd en resulteert deze in een precieze beschrijving van de optische data. Uit deze optische data, konden schalings exponenten bepaald worden, die het oppervlakte beschrijven in de initiële fase van patroon vorming voor verschillende substraat temperaturen. Voor een toenemende substraat temperatuur, worden er grotere lengte schalen waargenomen voor het gestructureerde oppervlak, hoewel de ontwikkeling in tijd zich identiek gedraagt.

Door de polaire hoek van inval van de ionen bundel naar 61.5° te veranderen, worden de gevormde structuren op het oppervlak twee dimensionaal, d.w.z. de strepen worden uitgerekte putjes. In hoofdstuk 5 hebben we RAS gebruikt om de ontwikkeling van deze structuren te volgen. In tegenstelling tot de optische spectra gemeten op de groeven, vertonen de metingen op de uitgerekte putjes resonanties in beide richtingen (i.e. positieve en negatieve pieken in de spectra). Dit betekent dat de één dimensionale benadering gebruikt voor het beschrijven van de groeven, niet meer voldoet in deze situatie. Daarom hebben we een twee dimensionaal RRT model gebruikt, om de periodiciteit en ruwheid in beide richtingen te beschrijven. Zowel een Gaussisch model, als een fysisch meer realistisch Edwards-Wilkinson model zijn gebruikt in het RRT model. De beschrijving met het Gaussische model beschrijft de metingen het best en laat zien dat de gemiddelde periodiciteit tussen de putjes parallel aan de ionen bron altijd groter is dan de periodiciteit loodrecht op de ionen bron. Beide richtingen groeien op een vergelijkbare manier, maar na verzadiging van de anisotrope ruwheid, wordt de ordening in de richting van de ionen bundel slechter.

Door de polaire hoek van inval van de ionen bundel naar 80° te veranderen, worden er bijna perfecte groeven gevormd. De periodiciteit van deze erg nauwe groeven is kleiner dan 200nm en daarom is dezelfde analyse als voor de groeven die gevormd worden onder een hoek van inval van 70° niet mogelijk. We laten zien dat voor deze kleine periodiciteiten, de sterkte van de resonantie afhankelijk is van periodiciteit en ruwheid van het oppervlak en dat het daarom niet mogelijk is om deze eigenschappen afzonderlijk af te leiden. Echter, de resonantie kan beschreven worden met een scheve Lorentz functie, wat een kwantitatieve analyse mogelijk maakt. De breedte van de functie verandert, wat een indicatie is voor de verandering van de diëlektrische functie door ruwheid op een kleine lengte schaal. Dit impliceert dat de daadwerkelijke diëlektrische functie van zilver aan het oppervlak lichtelijk verandert, door de reductie van de vrije weglengte voor elektronen, door ruwheid op een kleine lengte schaal.

In het laatste hoofdstuk 7, bestuderen we de patroon vorming door depositie bij scherende inval, als functie van bedekking. Voor depositie onder scherende inval ontstaan er langgerekte structuren. De anisotropie van het oppervlak wordt versterkt door een extra aantrekkende kracht tussen het oppervlak en inkomende atomen ('steering'). Aangezien de typische grootte van de structuren ver beneden 200nm is in beide richtingen, verwachten we alleen een netto resonantie piek op de oppervlakte plasmon energie. Uit simulaties weten we dat er een omslagpunt is voor de anisotropie voor een bepaalde bedekking. Echter, initiële experimenten laten een complexe combinatie van resonantie pieken zien, die wijzen op verschillende peroidiciteiten op het oppervlak. De omslag van de resonantie op de plasmon energie is niet waargenomen. Er zijn daarom meer experimenten nodig onder andere experimentele omstandigheden.

# List of publications

[1] **F. Everts**, H. Wormeester and B. Poelsema “Anomalous anisotropy in athermal Bradley-Harper roughening of Cu(001)” Phys. Rev. B **82**, 081415(R) (2010)
**Chapter 3**

[2] **F. Everts**, H. Wormeester and B. Poelsema “Optical anisotropy induced by ion bombardment of Ag(001)” Phys. Rev. B **78**, 155419 (2008)
**Chapter 4**

[3] **F. Everts**, H. Wormeester and B. Poelsema “Optical characterisation of the evolution of ion induced anisotropic nanopatterns on Ag(001)” submitted to PRB
**Chapter 5**

[4] H. Wormeester, **F. Everts** and B. Poelsema “Plasmon resonance shift during grazing incidence ion sputtering on Ag(001)” accepted in Thin Films as 5th ICSE article
**Chapter 6**

[5] F.L.W. Rabbering, H. Wormeester, **F. Everts** and B. Poelsema “Quantitative understanding of the growth of Cu/Cu(001) including the determination of the Ehrlich-Schwoebel barrier at straight steps and kinks” Phys. Rev. B **79**, 075402 (2009)

# Dankwoord

Hoewel alleen mijn naam aan de voorkant van dit boekje staat, is dit proefschrift uiteraard niet door mij alleen tot stand gekomen. Een promotie onderzoek succesvol afronden is een hels karwei en ik ben daarom blij dat ik er de afgelopen 4 jaar niet alleen voor stond. Er zijn veel mensen die een bijdrage hebben geleverd en daar ben ik ze erg dankbaar voor. Enkelen wil ik op deze plek bij naam noemen.

Bene, allereerst wil ik jou als promotor en groepsleider bedanken voor het gestelde vertrouwen in mij en de mogelijkheid die je mij hebt geboden om een promotie onderzoek te kunnen doen. Ik heb veel geleerd van jouw altijd kritische blik op mijn resultaten en de inhoudelijke discussies die we gevoerd hebben. Bedankt voor de prettige samenwerking, zowel inhoudelijk als op persoonlijk vlak.

Herbert, jou wil ik bedanken voor de dagelijkse begeleiding. Vooral het enthousiasme als er nieuwe resultaten behaald werden, maar ook de handigheid bij het oplossen van problemen in het lab zullen me bij blijven. Als experimenten even niet liepen zoals verwacht, had je altijd 1001 ideeën klaar staan om het op te lossen of te omzeilen.

Experimenteel onderzoek kan niet gedaan worden zonder een gedegen technische ondersteuning. Dit geldt zeker voor het zelf bouwen van een UHV systeem. Gelukkig beschikt de groep over twee bekwame technici. Herman, ik wil je ontzettend bedanken voor de vele uren die je in mijn systeem hebt gestoken. Vanaf het ontwerpen tot en met het daadwerkelijke opbouwen, je was bij alles erg betrokken en stond altijd klaar met raad en daad. Als het even tegen zat, bleef je toch optimistisch. Ook op persoonlijk vlak was het erg prettig om met je samen te werken.

Hans, ook jou wil ik bedanken voor de vele uren die je hebt besteed aan mijn systeem. Jouw vaardigheden in de werkplaats en met gereedschap hebben me heel wat uurtjes en frustratie bespaard. Als ik weer eens iets aangepast of gerepareerd moest hebben, stond je direct klaar en had je het vaak al gedaan voordat ik het hoefde te vragen. Ook met het ophalen van mijn nieuwe bank met jouw auto en de hulp om hem drie verdiepingen omhoog te sjouwen was ik erg blij.

Niet alleen het opbouwen van het nieuwe UHV systeem, maar ook het afbreken van het oude systeem (Dikke Bertha) was een enorme klus. Ik ben dan ook erg blij dat Marc precies op het goede moment stage kwam lopen en zin had om mij hiermee te helpen. Marc, bedankt voor de enorme hulp hiermee. Niets was je teveel en je bent letterlijk voor mij door het stof gegaan. Zonder jou was ik hier minstens twee keer zo lang mee bezig geweest. Naast de technische zaken, brengt promoveren ook een hoop administratieve taken met zich mee. Gelukkig nam Rianne dit voor haar rekening, zodat ik hier weinig omkijken naar had. Rianne, bedankt!

Ook wil ik de mensen bedanken waar ik mee samen heb gewerkt tijdens het afstuderen. Frits, mede dankzij jouw grenzeloze enthousiasme tijdens mijn afstudeerproject ben ik aan dit onderzoek begonnen en tot dit resultaat gekomen. En Tjeerd, als studenten waren we al betrokken bij elkaars onderzoek en dat is eigenlijk niet veranderd tijdens het promoveren. Het was erg prettig om een klankbord te hebben, op zowel fysisch als persoonlijk vlak. Ik wens je veel succes met het afronden van jouw onderzoek.

In de loop van de jaren heb ik het kantoor moeten delen met een aantal collega's. Gelukkig heerste er altijd een prettige werksfeer. De eerste tijd heb ik het kantoor gedeeld met Arie en Georgiana. Bedankt voor de leuke gesprekken en vooral de gezellige lunches. Later heb ik het kantoor met Arzu, Daniël, Maciej en Yogita gedeeld. Niet alleen in het kantoor, maar ook in het lab was het prettig met jullie samen te werken. Bedankt!

Verder wil ik de hele vakgroep bedanken voor de prettige sfeer, zowel tijdens als buiten werktijd. Met name denk ik met veel plezier terug aan het spelen in de vakgroepband. Daniël, Tijs, Amir, Arzu en Robbin, hartelijk bedankt hiervoor. Als we langer de tijd hadden gehad, weet ik zeker dat we waren doorgebroken!

Een stimulerende werkomgeving alleen is niet genoeg. Een promotieonderzoek staat natuurlijk niet op zichzelf en ik was dan ook nooit zover gekomen zonder de onvoorwaardelijke steun van mijn ouders. Mam, pap, hartelijk bedankt voor het vertrouwen en de steun die jullie mij mijn hele leven al geven!

Finishing the research and writing the thesis is the most difficult part. Fortunately, there was someone that kept me going during those tough times. Vindya, I would like to thank you for being so supportive and understanding. Although Sri Lanka is far away, you couldn't be closer to me.